Engineering Structures 208 (2020) 109917

Contents lists available at ScienceDirect

Engineering Structures

journal homepage: www.elsevier.com/locate/engstruct

Design method of structural retrofitting using viscous dampers based on elastic–plastic response reduction curve

Hua Shen[a,b], Ruifu Zhang[a,*], Dagen Weng[a], Qingzi Ge[c], Chao Wang[a], Md Mofakkharul Islam[a]

[a] Department of Disaster Mitigation for Structures, Tongji University, Shanghai 200092, China
[b] College of Civil Engineering, Nantong Vocational University, Nantong 226007, China
[c] Sichuan Institute of Building Research, Chengdu 610081, China

ARTICLE INFO

Keywords:
Viscous damper
Design method
Elastic–plastic response reduction curve
Energy dissipation
Passive control

ABSTRACT

Installation of viscous dampers has been demonstrated to be an effective method to perform seismic retrofitting of a structure. However, most of the existing design methods are based on the elastic stage of the primary structure. The proposed study presents an alternate method for retrofit design of a structure using viscous dampers whilst considering inelastic behaviour of the primary structure. The said method makes use of the elastic–plastic response reduction curve (EPRRC) to reflect the relationship between characteristic parameters of the viscous damper, supporting brace, and response of the viscous-damper-equipped primary structure. Use of this method ensures that reduction in storey drift as well as shear force is simultaneously realized within the EPRRC coincident reduction region. Thus, parameters concerning the required dampers and supporting braces can be obtained from EPRRC in accordance with target performances of the damped structure. Comparison between a traditional elastic response reduction curve (ERRC) and EPRRC indicates that ERRC tends to overestimate the performance of damped structures. Nonlinear time-history analysis was performed to verify the effectiveness of the proposed method when applied to a benchmark model. Additionally, probabilistic reliability of the said method was determined via incremental dynamic analysis. Results demonstrate that the proposed design method can effectively satisfy design requirements under different seismic intensities.

1. Introduction

Passive energy-dissipation technology has been demonstrated as an effective method for structural control [1–5]. Viscous dampers—a type of energy-dissipation device—have been widely employed to provide wind and seismic protection to building structures [6–13]. Modern viscous dampers are characterized by excellent properties, including temperature insensitivity [14], velocity dependence, zero storage stiffness in the low-frequency range and low-displacement activation [15]. Moreover, a mechanical phenomenon, called “out-of-phase”, forms an important characteristic of viscous dampers by virtue of which occurrence of the maximum damping force does not coincide with that of the maximum displacement amplitude [8]. Via appropriate design and fabrication, viscous dampers can demonstrate realization of near-perfect sealing, and they possess no parts that wear out or deteriorate with time during the expected lifetime of a device [16].

To employ viscous dampers in actual engineering structures, use of an appropriate design methodology assumes great importance. Certain design methods are developed to facilitate retrofitting of existing structures using viscous dampers. Constantinou and Symans [15] employed the response-spectrum approach to design structures equipped with viscous dampers, and based on the elastic response reduction curve (ERRC) a general design method was presented by the Japan Society of Seismic Isolation [2]. Weng et al. [17] proposed a simplified design method for designing viscous dampers to perform retrofitting of an earthquake-damaged reinforced concrete frame. In [18], a modified design procedure for velocity-dependent dampers has been delivered by enhancing the accuracy and reliability of linear static and dynamic procedures of FEMA273. An extended method has been proposed by Palermo et al. [19] to be applied to structures ranging from those of the shear type to generic moment-resisting frames, based on the method presented by Silvestri et al. [20] that involves use of a five-step procedure for seismic design of a main linear structure equipped with viscous dampers via use of time history analysis. Subsequently, Silvestri et al. [21] proposed use of a direct five-step procedure employing practical tools to identify mechanical characteristics of viscous dampers to achieve target performance levels. In addition, Dall’Asta et al. [22] systematically analysed the effect of variations in viscous-damper

* Corresponding authors.
E-mail address: zhangruifu@tongji.edu.cn (R. Zhang).

https://doi.org/10.1016/j.engstruct.2019.109917
Received 4 September 2018; Received in revised form 9 November 2019; Accepted 9 November 2019
Available online 26 November 2019
0141-0296/

Acronyms

ERRC	elastic response reduction curve
EPRRC	elastic–plastic response reduction curve
SPS	short-period structure
MPS	medium-period structure
CRR	coincidental reduction region
NCRR	non-coincidental reduction region
PGA	peak ground acceleration
TSPP	target structural performance point
IDA	incremental dynamic analysis

properties on probabilistic system response as well as risks involved therein to improve the rationality of design. Design methods proposed in the above-cited studies are all based on the consideration of elastic behaviour of the primary structure. However, in accordance with performance-based design requirements, structural responses must also meet performance targets when subjected to different seismic intensities. Primary structures may inevitably demonstrate operation within the plastic range in the event of occurrence of a high-intensity earthquake. The capacity-spectrum [23,24] and direct displacement-based design methods [25–27] have, therefore been developed to facilitate design of structures equipped with viscous dampers whilst accounting for the plastic behaviour of primary structures. Use of these methods, however, requires performing an iterative calculation or trial-and-error process to determine the supplemental damping provided by viscous dampers. Hejazi et al. [28] presented a trial-and-error-based design method that considered yielding mechanisms of reinforced-concrete structures subject to seismic excitation whilst also incorporating non-linear dynamic analysis. Guo and Christopoulos [29] presented a performance spectrum-based method for structures equipped with passive supplemental damping systems. This method, however, was only suitable for use with linear viscous dampers and required performance spectra to be generated in advance, which is complicated.

Some extant researches [30–46] proposed use of optimization design methods concerning installation of viscous dampers. Using genetic algorithm and nonlinear response history analysis, Huang [47] proposed use of a practical framework to facilitate optimization of the distribution of viscous dampers within moment-resisting frames by reducing large drifts generated upon occurrence of intense seismic activity. Using the linear-approximation method, Altieri et al. [48] presented reliability-based optimum design of primary structures employing viscous dampers to reduce the probability of structural failure whilst incurring minimum cost of dampers. Use of these optimum design methodologies demonstrates attainment of satisfactory results to meet the performance target under certain constraint conditions. Such methods usually requires significant amounts of computation time and labour. While they are too complicated to be used in a real structural designs, results obtained can, nonetheless, be used as reference to make good design decisions concerning practical design. It is, therefore, necessary to develop a simple and practical method for design of a structure equipped with viscous dampers and operating within the elastic–plastic range of primary structures.

The proposed study presents a method for design of a structure equipped with viscous dampers based on the elastic–plastic response reduction curve (EPRRC)—an extension of ERRC—that accounts for plastic behaviour of the primary structure. Use of the said method serves to simultaneously reduce both displacement and shear force within the coincidental reduction region (CRR), as observed in both ERRC and EPRRC. Differences between EPRRC and ERRC of viscous dampers have been compared, and the detailed design process has been appropriately explained. Finally, an example of application of the proposed method has been presented, and the method's effectiveness has been evaluated via non-linear time-history analysis, and the probabilistic reliability is further identified by using incremental dynamic analysis (IDA).

2. Response reduction curve

2.1. Analytical model for primary structures equipped with viscous dampers

In practical applications, viscous dampers are commonly connected to the primary structure by means of a supporting brace with sufficient stiffness. The Maxwell model, which is typically employed in structural design, adequately reflects the mechanical behaviour of viscous dampers at the design level [49]. It is obviously different from the Kelvin model for viscoelastic damper [50] and the hysteretic model for metallic yielding damper [51]. An original model of a primary structure with a viscous damper has been illustrated in Fig. 1(a). In this model, the viscous damper and supporting brace are placed in series with one another whilst being parallel to the primary structure. Parameters C_d and K_d refer to the damping coefficient and internal elastic stiffness of the viscous damper, respectively, while K_b and K_f denote elastic stiffness of the supporting brace and primary structure, respectively. Lastly, M denotes lump mass of the single-degree-of-freedom model. Since K_d and K_b are arranged in series, they can be replaced, in the original model, by an equivalent supporting brace stiffness K_b^* and represented

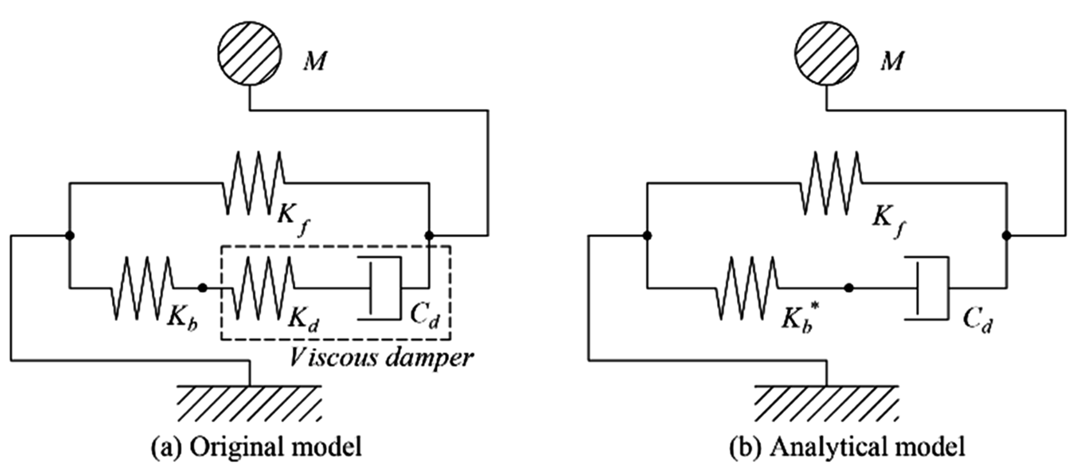

Fig. 1. Models of primary structure with viscous damper.

as an analytical model, as depicted in Fig. 1(b) and mathematically expressed as

$$K_b^* = \frac{K_b K_d}{K_b + K_d}. \tag{1}$$

Based on connections of the said analytical model, a corresponding force–displacement relationship could be obtained, as illustrated in Fig. 2. The damping force of the viscous element F_d must always equal that of the equivalent supporting brace F_b^* owing to the viscous element of the damper being connected to the equivalent supporting brace in series. The force–displacement relationship of the additional system, is depicted Fig. 2(a) with the system comprising a viscous element and an equivalent supporting brace. Because the additional system is arranged in parallel with respect to the primary structure, displacement of the additional system u_a must always equal that of the primary structure u_f. The overall force–displacement relationship of the analytical model can be obtained as described in Fig. 2(b).

The constitutive equation of the viscous element between the damping force F_d and relative velocity v_d between two ends of the viscous element can be expressed as [1]

$$F_d = C_d\ |v_d|^{\alpha}\mathrm{sign}(v_d) \tag{2}$$

where α denotes the relative-velocity exponent—usually between 0.15 and 1 [48]; it is directly related to the geometric shape of the hysteretic loop. The function of sign() denotes the signum function. To express the relationship between the maximum damping force $F_{d,max}$ and maximum displacement $u_{d,\max}$ of the viscous element, nominal stiffness of the viscous element K_d' has been used, as depicted in Fig. 2. Using Eq. (2), an expression for K_d' can be derived as follows.

$$K_d' = \frac{F_{d,\max}}{u_{d,\max}} = \frac{C_d\,(\omega_d^{\alpha}\,u_{d,\max}^{\alpha})}{u_{d,\max}} = \frac{C_d\,\omega_d^{\alpha}}{u_{d,\max}^{1-\alpha}} \tag{3}$$

where ω_d denotes angular frequency of the viscous element.

It is well known that when $\alpha = 0$, the force–displacement relationship of the viscous element assumes a form similar to that of the friction damper, whereas the condition $\alpha = 1$ corresponds to a linear viscous damper, in accordance to Eq. (2). Hysteretic loops corresponding to the friction and linear viscous dampers, therefore, assume the rectangular and elliptical shapes, respectively. Shapes of these viscous-element hysteretic loops are depicted in Fig. 2(a) for values of α between 0 and 1. According to [2], once responses from the analytical model have been obtained for $\alpha = 0$ and $\alpha = 1$, responses for other cases with α values in the range of $0.15 < \alpha < 1$ can be calculated based on results obtained for $\alpha = 0$ and $\alpha = 1$ using interpolation.

2.2. Response reduction indexes

The displacement reduction R_d and pseudo-acceleration (base-shear) reduction R_{pa} indexes [51] were introduced to quantify the difference between seismic responses of the primary structure with and without viscous dampers. These indexes can be expressed as below based on the relationship between the peak elastic displacement S_d, pseudo-velocity S_{pv}, and pseudo-acceleration S_{pa} by considering characteristics of the pseudo-velocity spectrum and pseudo-acceleration spectrum in the range of fundamental periods [52].

(i) For short-period structures (SPSs)

$$R_d = \frac{S_d\,(T_{eq},\,\zeta_{eq})}{S_d\,(T_f,\,\zeta_0)} = D_\zeta\left(\frac{T_{eq}}{T_f}\right)^2, \tag{4}$$

$$R_{pa} = \frac{S_{pa}\,(T_{eq},\,\zeta_{eq})}{S_{pa}\,(T_f,\,\zeta_0)} = R_d\left(\frac{T_f}{T_{eq}}\right)^2 \tag{5}$$

where T_{eq} and T_f denote the equivalent period of analytical model and the period of the primary structure, respectively; D_ζ denotes the average reduction value of the seismic response [2].

(ii) For medium-period (MPSs) and long-period structures

$$R_d = \frac{S_d\,(T_{eq},\,\zeta_{eq})}{S_d\,(T_f,\,\zeta_0)} = D_\zeta\frac{T_{eq}}{T_f}. \tag{6}$$

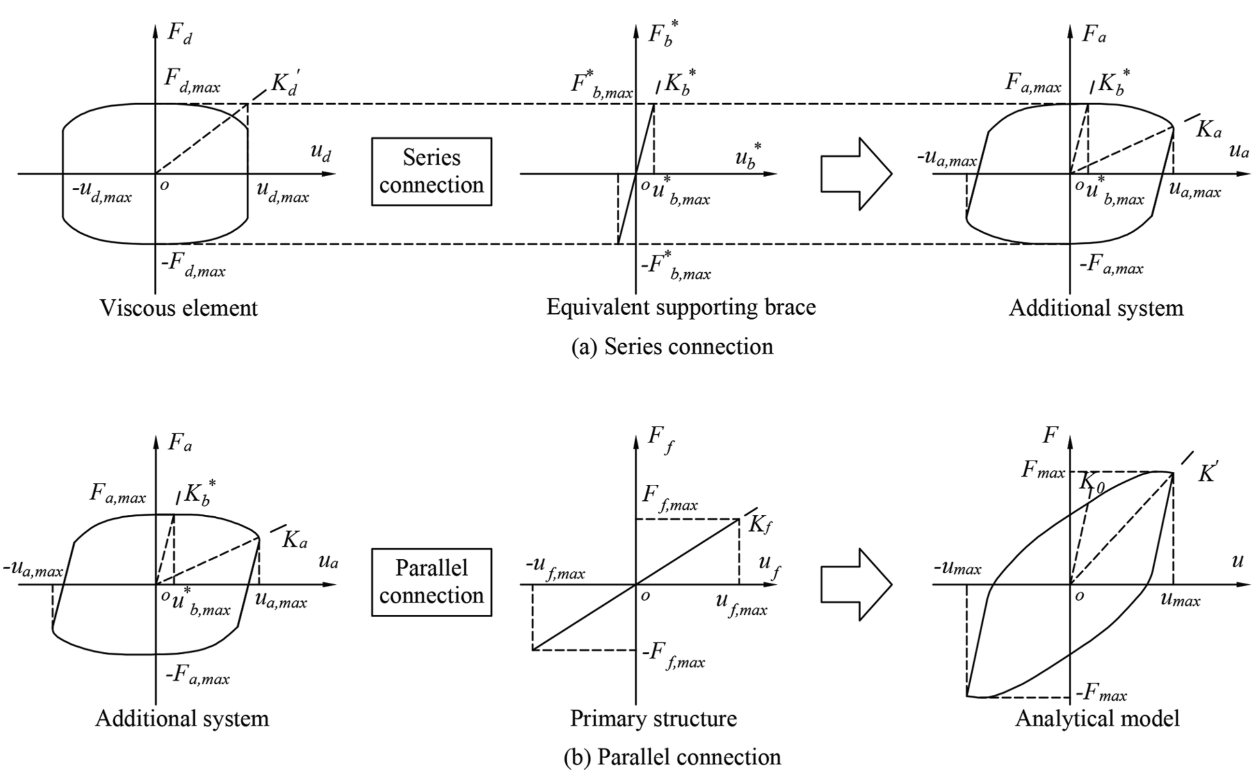

Fig. 2. Force–displacement relationships for analytical model.

The formula for R_{pa} remains identical to Eq. (5).

The parameter R_{pa} denotes the shear-force reduction index corresponding to maximum displacement of the analytical model in accordance with the response spectrum theory; however, the out-of-phase phenomenon, as previously mentioned, causes the maximum shear force of the viscous damper to not occur concurrently with the maximum displacement, especially for cases with $\alpha = 1$. The acceleration reduction index $R_a|_{\alpha=1}$ can, therefore, be expressed as [2]

$$R_a|_{\alpha=1} = \sqrt{1 + 4\zeta_{eq}^2} R_{pa}|_{\alpha=1} \tag{7}$$

where ζ_{eq} denotes equivalent damping ratio of the analytical model.

For cases with $\alpha = 0$, the viscous element can be considered as a friction element. Consequently, the maximum shear force of the viscous damper can be synchronized with the maximum displacement. Thus, the acceleration reduction index $R_a|_{\alpha=0}$ for $\alpha = 0$ can be expressed as

$$R_a|_{\alpha=0} = R_{pa}|_{\alpha=0}. \tag{8}$$

For α values in the range of 0–1, values of R_d and R_a can be calculated as follows using non-linear interpolation [2].

$$R_d = R_d|_{\alpha=0} - (R_d|_{\alpha=0} - R_d|_{\alpha=1})\sqrt{\alpha(2-\alpha)}, \tag{9}$$

$$R_a = R_{pa}|_{\alpha=0} - (R_{pa}|_{\alpha=0} - R_a|_{\alpha=1})\sqrt{\alpha(2-\alpha)}. \tag{10}$$

Prior to evaluating R_d and R_a, it is necessary to calculate values of T_{eq} and ζ_{eq}.

2.3. Calculation of T_{eq} and ζ_{eq}

2.3.1. $\alpha = 0$

For $\alpha = 0$, the geometric shape of the hysteretic loop for the viscous element is rectangular, as depicted in Fig. 3. As previously discussed, the viscous element was arranged in series with the equivalent supporting brace, and the additional system was arranged in parallel with regard to the primary structure. A step-by-step transformation process of the force–displacement relationship of the analytical model has been illustrated in Fig. 3. Equivalent period of analytical model $T_{eq}|_{\alpha=0}$ can, therefore, be calculated as

$$T_{eq}\Big|_{\alpha=0} = T_f\sqrt{\frac{K_f}{K_a + K_f}} = T_f\sqrt{\frac{1+m}{1+m+p}} \tag{11}$$

where $m = K_b^*/K_d'$ denotes the ratio of stiffness of the equivalent supporting brace to nominal stiffness of the viscous element; $p = K_b^*/K_f$ denotes stiffness ratio of the equivalent supporting brace to the primary structure. Stiffness of the additional system K_a has been described in Appendix A.

Equivalent damping ratio of the analytical model $\zeta_{eq}|_{\alpha=0}$ comprises two components— inherent damping ratio ζ_0, which is usually set to 5% and 2% for reinforced-concrete and steel structures, respectively, and hysteretic damping ratio of the additional system $\zeta_a|_{\alpha=0}$, which can be expressed as

$$\zeta_{eq}|_{\alpha=0} = \zeta_0 + \zeta_a|_{\alpha=0} \tag{12}$$

where $\zeta_a|_{\alpha=0}$ can be calculated as [53]

$$\zeta_a\Big|_{\alpha=0} = \frac{E_D}{4\pi E_s}. \tag{13}$$

Parameters E_D and E_S denote the area enclosed by the hysteretic loop under conditions of maximum displacement and maximum stored potential energy, respectively, corresponding to the analytical model. Thus, $\zeta_a|_{\alpha=0}$ can be expressed as

$$\zeta_a\Big|_{\alpha=0} = \frac{2p(\mu_a - 1)}{\pi p \mu_a} \tag{14}$$

where μ_a can be defined as the maximum nominal ductility coefficient of the additional system expressed as

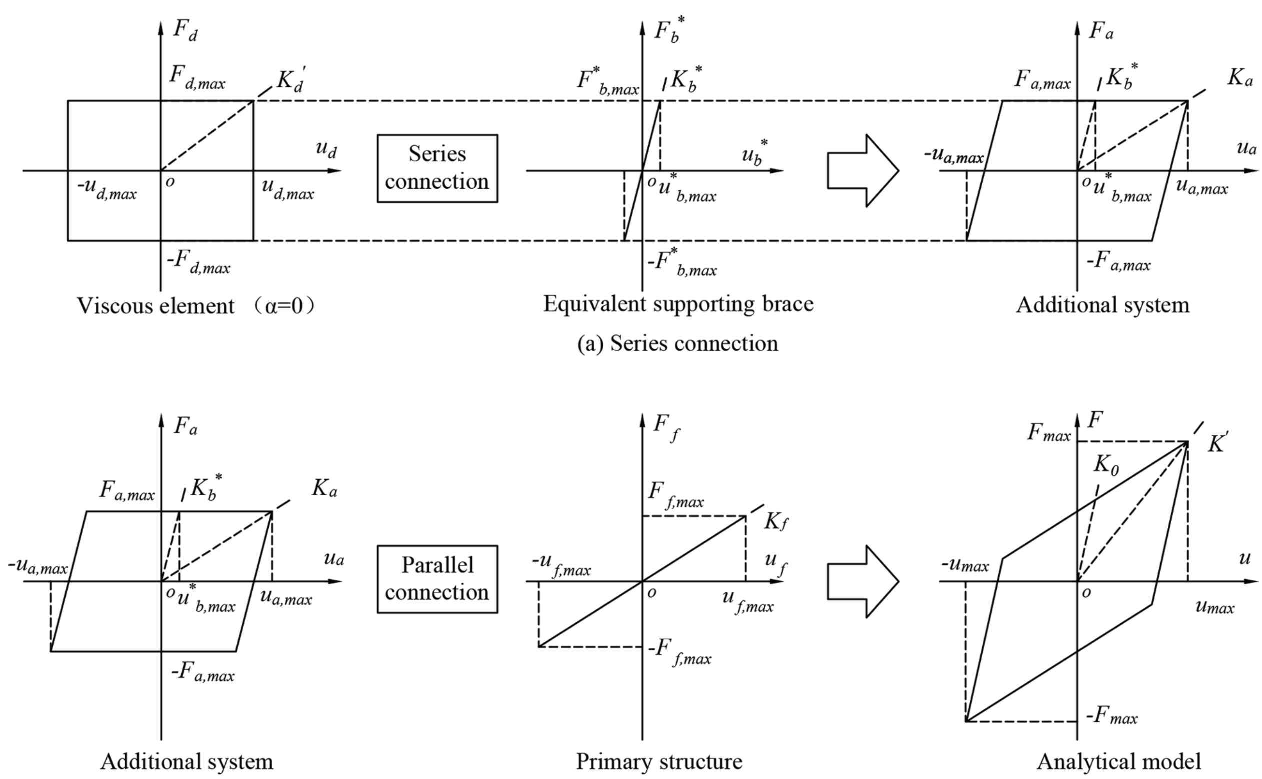

Fig. 3. Force–displacement relationships for analytical model ($\alpha = 0$).

$$\mu_a = \frac{u_{a,\max}}{u^*_{b,\max}} = \frac{u_{d,\max} + u^*_{b,\max}}{u^*_{b,\max}} = m + 1. \tag{15}$$

Under seismic excitation, the maximum nominal ductility coefficient varies from 1 to μ_a owing to randomness of the seismic response; consequently, $\zeta_{eq}|_{\alpha=0}$ can be expressed as

$$\zeta_{eq}\Big|_{\alpha=0} = \zeta_0 + \frac{1}{\mu_a}\int_1^{\mu_a} \zeta_a|_{\alpha=0}(\mu)d\mu = \zeta_0 + \frac{2}{\pi(1+m)n}\ln\frac{1+mn}{(1+m)^n}, \tag{16}$$

$$n = \frac{1}{1+p}. \tag{17}$$

2.3.2. The case $\alpha = 1$

For $\alpha = 1$, the hysteretic loop of the viscous element assumes an elliptical shape, as depicted in Fig. 4. Similar to the process described above, equivalent period of the analytical model $T_{eq}|_{\alpha=1}$ can be expressed as

$$T_{eq}\Big|_{\alpha=1} = T_f\sqrt{\frac{K_f}{K_a + K_f}} = T_f\sqrt{\frac{1+m^2}{1+m^2+p}} \tag{18}$$

Stiffness K_a of the additional system has been appropriately described in Appendix A.

In accordance with Eq. (13), for $\alpha = 1$, the hysteretic damping ratio for the additional system $\zeta_a|_{\alpha=1}$ takes the form

$$\zeta_a\Big|_{\alpha=1} = \frac{1}{2}\cdot\frac{qm^2}{1+p+m^2} \tag{19}$$

where $q = K_d'/K_f$ denotes the ratio of nominal stiffness of the viscous element to stiffness of the primary structure. Given the randomness of seismic response, an equivalent damping ratio of the analytical model $\zeta_{eq}|_{\alpha=1}$ can be expressed as

$$\zeta_{eq}|_{\alpha=1} = \zeta_0 + 0.8\zeta_a|_{\alpha=1} \tag{20}$$

where 0.8 denotes a reduction factor [54].

2.4. ERRC

Substituting Eqs. (11) and (18) into Eq. (4) and considering $m = p/q$, $R_d|_{\alpha=0}$ and $R_d|_{\alpha=1}$ for SPS can, respectively, be expressed as

$$R_d\Big|_{\alpha=0} = D_\zeta\cdot\frac{p+q}{p+q+pq}, \tag{21}$$

$$R_d\Big|_{\alpha=1} = D_\zeta\cdot\frac{p^2+q^2}{p^2+q^2+pq^2}. \tag{22}$$

Substituting Eqs. (21) and (22) into Eq. (5) and considering $m = p/q$, $R_{pa}|_{\alpha=0}$ and $R_{pa}|_{\alpha=1}$ for SPS can be expressed as

$$R_{pa}|_{\alpha=0} = R_{pa}|_{\alpha=1} = D_\zeta. \tag{23}$$

Subsequently, combining Eqs. (7) and (23), $R_a|_{\alpha=1}$ can be calculated as follows,

$$R_a\Big|_{\alpha=1} = D_\zeta\sqrt{1+4\zeta_{eq}^2}. \tag{24}$$

Combining Eqs. (21)–(24) with Eqs. (9) and (10), R_d and R_a can be expressed as functions of p and q, respectively. For MPS, a long-period structure with viscous damper can also be derived similar to SPS. As this process only considers operation within the elastic range of the primary structure, the $R_d - R_a$ curve is referred to as ERRC [51].

For example, the design-response spectrum of the Chinese code for seismic design of a building [55] has been adopted to derive the ERRC. In this study, SPS ($0.1\ s < T \leqslant T_g$) and MPS ($T_g < T \leqslant 5\ T_g$), where T_g denotes the characteristic period of the design response spectrum, have been considered, since fundamental periods in most practical building structures lie within the range of $0.1\ s$ to $5\ T_g$. In accordance with Eqs.

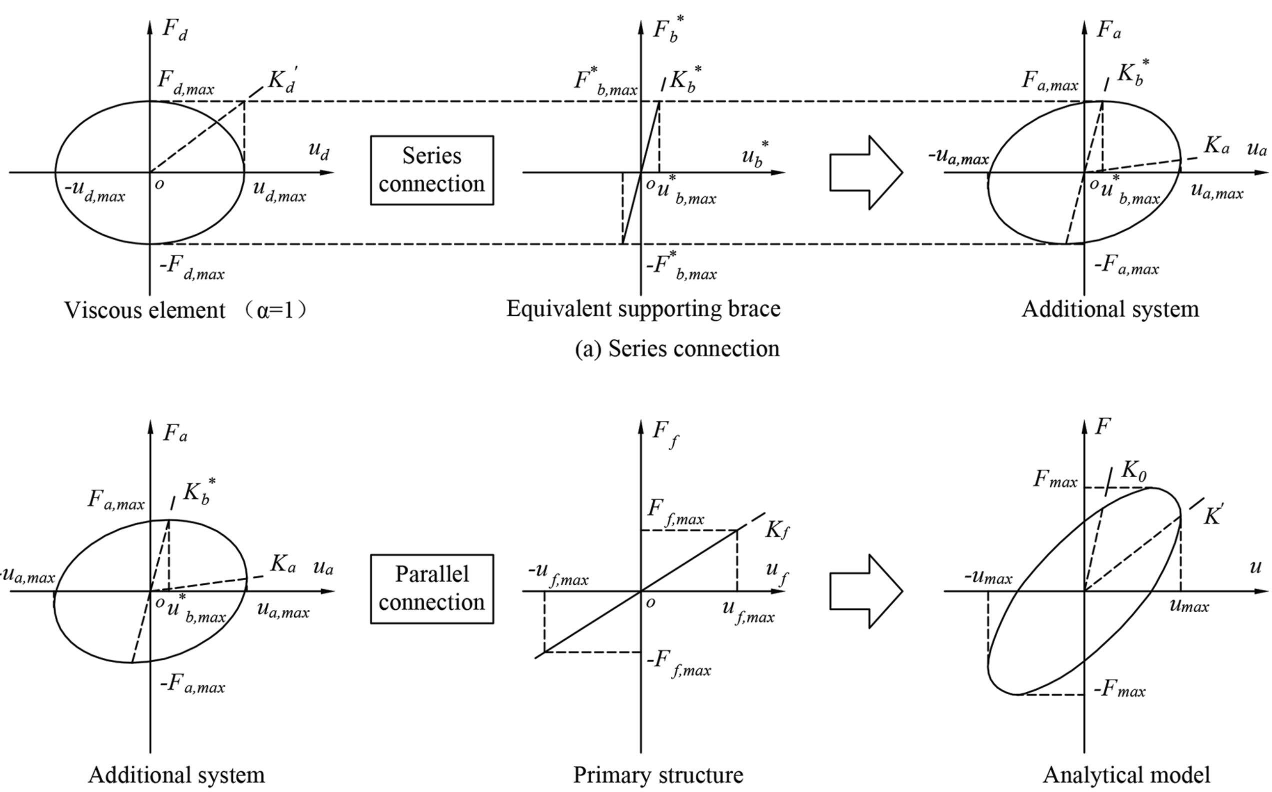

Fig. 4. Force–displacement relationships for analytical model ($\alpha = 1$).

(4) and (6), corresponding values of R_d for ERRCs can be obtained using following relations.

(i) For SPSs ($0.1\ s < T \leqslant T_g$), R_d can be expressed as:

$$R_d = \frac{S_d(T_{eq}, \zeta_{eq})}{S_d(T_f, \zeta_0)} = \frac{\eta_{2eq}}{\eta_{20}} \frac{T_{eq}^2}{T_f^2} \tag{25}$$

where η_{20} and η_{2eq} denote damping modification factors for ζ_0 and ζ_{eq}, respectively.

(ii) For MPSs ($T_g < T \leqslant 5\ T_g$), R_d can be expressed as

$$R_d = \frac{S_d(T_{eq}, \zeta_{eq})}{S_d(T_f, \zeta_0)} = \frac{\eta_{2eq}}{\eta_{20}} \left(\frac{T_{eq}}{T_f}\right)^{2-\gamma_{2eq}} \left(\frac{T_f}{T_g}\right)^{\gamma_{20}-\gamma_{2eq}} \tag{26}$$

where γ_{20} and γ_{2eq} denote exponential indexes for descending branches of ζ_0 and ζ_{eq}, respectively.

For cases wherein $\alpha = 0.2$, $\zeta_0 = 0.05$, $0.5 \leqslant p \leqslant 5$, $0 \leqslant q \leqslant 10$, and $T_f/T_g = 1.5$, ERRCs corresponding to SPS and MPS have been plotted in Fig. 5(a) and (b), respectively, in accordance with Eqs. (5), (25) and (26). The region with white background in Fig. 5 is referred to as the coincidental reduction region (CRR), wherein the displacement and shear-force acceleration are simultaneously reduced. Likewise, the region with grey background is called the non-coincidental reduction region (NCRR), wherein only the displacement is reduced. In practice, CRR is preferred by designers under certain conditions.

To ensure existence of constant q and increasing values of p, values of R_a and R_d for SPS decrease significantly, as depicted in Fig. 5(a), thereby implying that the effects of vibration control on displacement and acceleration both improve corresponding to an increase in stiffness of the equivalent supporting brace. On the other hand, for constant p and increasing values of q, the value of R_a first decreases with subsequent increase, whereas that of R_d first undergoes a rapid decrease followed by minimal decrements. This trend demonstrates that for a small nominal stiffness of the viscous element, the effects of control on displacement and acceleration are enhanced with increase in stiffness; however, for a large nominal stiffness, the effect of control on displacement is minimal whereas that on acceleration is weakened with increase in stiffness. Further, all SPS ERRCs are located within CRR.

A comparison between Fig. 5(a) and (b) indicates similarity in overall trends with only minor differences. For increasing values of p and a small value of q, values of both R_a and R_d for MPS reduce; for a large value of q, the value of R_d decreases rapidly, whereas the R_a demonstrates minimal decrease. As the value of q further increases, R_a demonstrates an increase. This implies that a large nominal stiffness of the viscous element is preferred to control the effect on MPS displacement compared to acceleration. Meanwhile, under identical conditions, CRR for MPS is significantly smaller to that for SPS. This indicates that suitable parameter values for SPS are easier to obtain compared to MPS.

2.5. EPRRC

ERRC directly reflects the effect of vibration control on a primary structure with viscous dampers within the elastic range of the primary structure. The ERRC concept can be effectively applied to the design of structures equipped with viscous dampers and subjected to frequent seismic events. However, primary structures may inevitably enter the inelastic range of operation under moderate or severe seismic activity. Once the primary structure enters the inelastic range of operation, its dynamic properties tend to change, and the structure becomes a special damper to dissipate input seismic energy via plastic deformation. Obviously then, ERRC becomes unsuitable for use in such conditions. Although a performance-based seismic design requires that a structure meets corresponding performance targets under different intensity-level seismic events, it is worthwhile that ERRC be modified to EPRRC to consider the plastic behaviour of primary structures.

2.5.1. Force–displacement relationship for inelastic primary structures

A bilinear model, as shown in Fig. 6, was adopted in this study to simulate the inelastic mechanical behaviour of primary structures. In the figure, the yielding force, yielding displacement, secant stiffness, and ratio of post-yielding stiffness are denoted by $F_{f,y}$, $u_{f,y}$, K_f', and β, respectively, while other parameters have been defined. Using the secant stiffness method, equivalent period of an inelastic primary structure T_f' can be calculated using the following relation.

$$T_f' = T_f\sqrt{\frac{K_f}{K_f'}} = T_f\sqrt{\frac{\mu_f}{1+\beta\mu_f-\beta}} \tag{27}$$

where $\mu_f = u_{max}/u_{f,y}$ denotes maximum ductility coefficient of the inelastic primary structure.

2.5.2. Calculation of T_{eq}' and ζ_{eq}'

The equivalent period T_{eq}' and equivalent damping ratio ζ_{eq}' of an inelastic analytical model can be derived to obtain EPRRC. For the derivation process of ERRC, these two parameters were calculated as follows for cases with $\alpha = 0$ and $\alpha = 1$.

(i) $\alpha = 0$

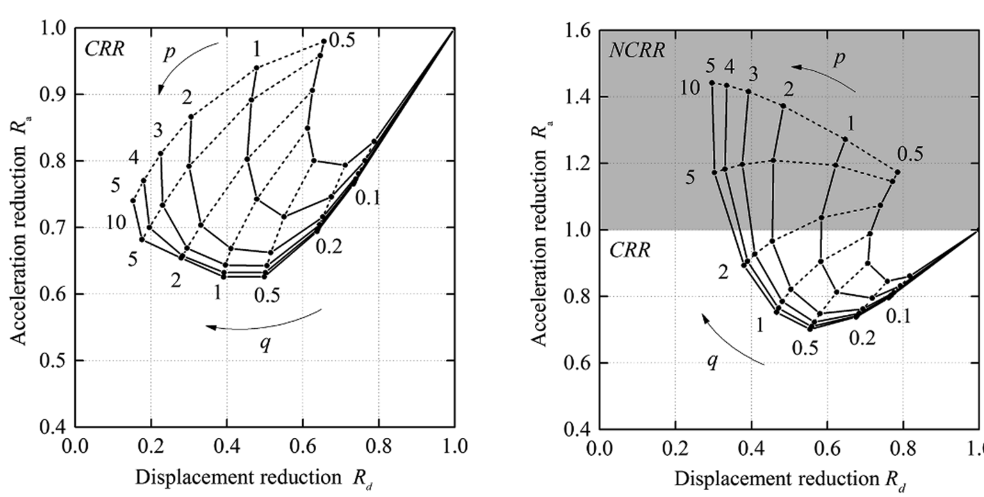

(a) SPS (b) MPS (T_f / T_g = 1.5)

Fig. 5. ERRCs corresponding to conditions ($\alpha = 0.2$; $\zeta_0 = 0.05$).

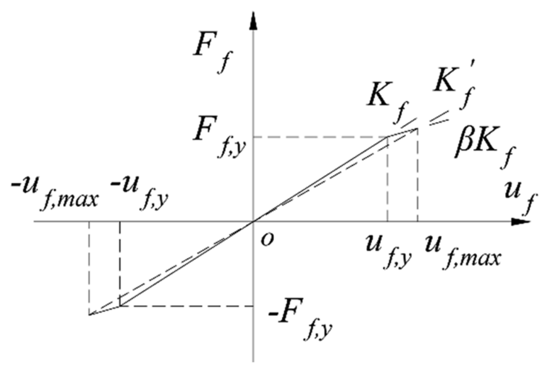

Fig. 6. Force–displacement relationship for inelastic primary structure.

For $\alpha = 0$ (Fig. 7), $T'_{eq}|_{\alpha=0}$ of the inelastic analytical model can be expressed as

$$T'_{eq}\Big|_{\alpha=0} = T'_f\sqrt{\frac{K'_f}{K_a + K'_f}} = T'_f\sqrt{\frac{1 + \beta\mu_f - \beta}{1 + \beta\mu_f - \beta + \frac{p}{1+m}\mu_f}} \tag{28}$$

here, stiffness K_a of the additional system has been described in detail in Appendix A.

During operation within the inelastic range, nonlinear hysteretic damping is generated within the primary structure to absorb seismic input energy. The total effective damping ratio, therefore, comprises three components—the inherent damping ratio ζ_0, nonlinear hysteretic damping ratio of the additional system ζ'_a, and that of the primary structure ζ'_f. The equivalent damping ratio $\zeta'_{eq}\Big|_{\alpha=0}$ of the inelastic analytical model can, therefore, be expressed as

$$\zeta'_{eq}\Big|_{\alpha=0} = \zeta_0 + \zeta'_a\Big|_{\alpha=0} + \zeta'_f\Big|_{\alpha=0} \tag{29}$$

For $\alpha = 0$ and $u_{a,\max} = u_{f,\max} = u_{\max}$, terms $\zeta'_a|_{\alpha=0}$ and $\zeta'_f\Big|_{\alpha=0}$ with μ_a and μ_f can be expressed as below through use of calculations described in Appendix B.

$$\zeta'_a\Big|_{\alpha=0} = \frac{2p(\mu_a - 1)}{\pi\mu_a[p + \eta + \beta(\mu_a - \eta)]} \tag{30}$$

$$\zeta'_f\Big|_{\alpha=0} = \frac{2\eta\rho(1 - \beta)(\mu_f - 1)}{\pi\mu_f[p + \eta + \beta\eta(\mu_f - 1)]} \tag{31}$$

$$\eta = u_{f,y}/u^*_{b,\max} \tag{32}$$

where ρ denotes the damping modification factor, as listed in Table 1.

Under seismic excitation, expressions for nonlinear hysteretic damping ratios ($\zeta'_a|_{\alpha=0}$ and $\zeta'_f\Big|_{\alpha=0}$) can be rewritten as follows to account for the randomness of seismic response by considering the maximum ductility coefficient to vary between 1 to μ_a and 1 to μ_f, respectively.

Table 1
Damping modification factor ρ referenced from ATC-40 [53].

Structural behaviour type	Feature of hysteretic loop	ρ
A	Full	1
B	Moderate	2/3
C	Poor	1/3

$$\begin{aligned}\zeta'_a\Big|_{\alpha=0} &= \frac{1}{\mu_a}\int_1^{\mu_a}\zeta'_a|_{\alpha=0}(\mu)d\mu \\ &= \frac{2p}{\pi r\mu_a}\left[\ln\frac{(\beta\mu_a + r)^{(r+\beta)/\beta}}{\mu_a} - \frac{r+\beta}{\beta}\ln(\beta + r)\right]\end{aligned} \tag{33}$$

$$\begin{aligned}\zeta'_f\Big|_{\alpha=0} &= \frac{1}{\mu_f}\int_1^{\mu_f}\zeta'_f|_{\alpha=0}(\mu)d\mu \\ &= \frac{2\eta\rho(1-\beta)}{\pi\mu_f(s-t)}\left\{\ln\frac{\mu_f}{[s(\mu_f - 1) + t]^{t/s}} + \frac{t}{s}\ln t\right\}\end{aligned} \tag{34}$$

$$r = p + \eta - \beta\eta \tag{35}$$

$$s = \beta\eta \tag{36}$$

$$t = p + \eta \tag{37}$$

(ii) $\alpha = 1$

For $\alpha = 1$ (Fig. 8), $T'_{eq}|_{\alpha=1}$ for an inelastic analytical model can be expressed as

$$T'_{eq}\Big|_{\alpha=1} = T'_f\sqrt{\frac{K'_f}{K_a + K'_f}} = T'_f\sqrt{\frac{1 + \beta\mu_f - \beta}{1 + \beta\mu_f - \beta + \frac{p}{1+m^2}\mu_f}} \tag{38}$$

with stiffness K_a of the additional system being described in Appendix A.

The equivalent damping ratio of the inelastic analytical model $\zeta'_{eq}\Big|_{\alpha=1}$ can be expressed as

$$\zeta'_{eq}\Big|_{\alpha=1} = \zeta_0 + \zeta'_a\Big|_{\alpha=1} + \zeta'_f\Big|_{\alpha=1}. \tag{39}$$

In accordance with Eq. (13) and $u_{a,\max} = u_{f,\max} = u_{\max}$, terms $\zeta'_a|_{\alpha=1}$ and $\zeta'_f\Big|_{\alpha=1}$ with μ_a and μ_f, respectively, can be expressed as follows with details concerning the derivation being presented in Appendix B.

$$\zeta'_a\Big|_{\alpha=1} = \frac{pm\sqrt{1 + m^2}}{2\eta\{[p + \beta(1 + m^2)]\mu_f + (1 - \beta)(1 + m^2)\}} \tag{40}$$

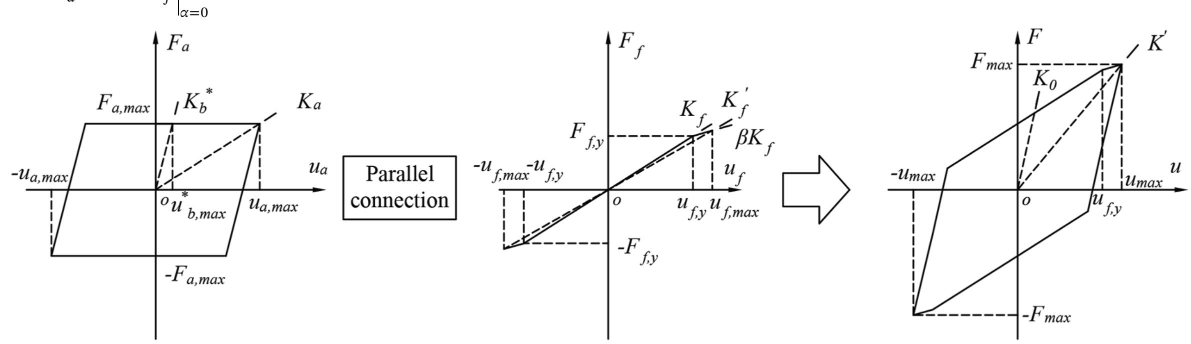

Fig. 7. Force–displacement relationships for inelastic analytical model ($\alpha = 0$).

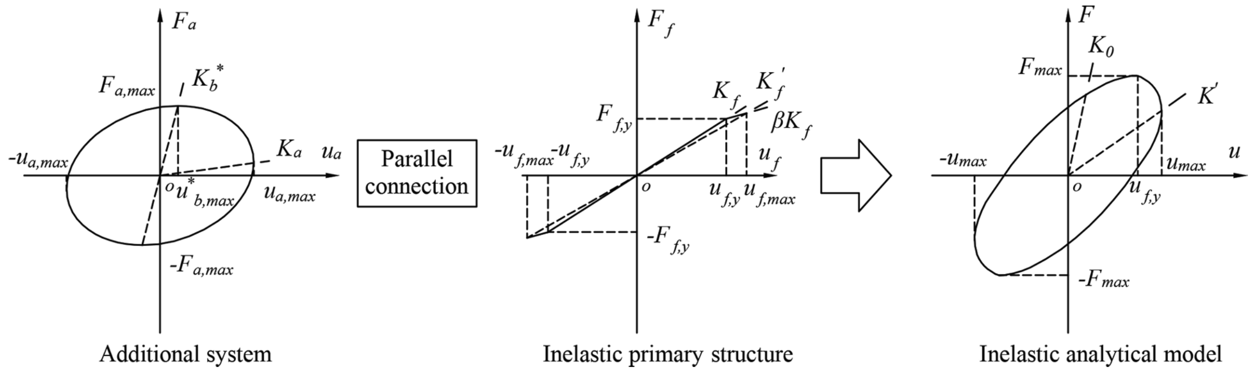

Fig. 8. Force–displacement relationships for inelastic analytical model ($\alpha = 1$).

$$\zeta'_f\Big|_{\alpha=1} = \frac{2\rho(1-\beta)(1+m^2)(\mu_f-1)}{\pi\mu_f(z\mu_f+w)} \tag{41}$$

$$w = (1-\beta)(1+m^2) \tag{42}$$

$$z = p + \beta(1+m^2) \tag{43}$$

Under seismic excitation, nonlinear hysteretic damping ratios $\zeta'_a|_{\alpha=1}$ and $\zeta'_f\Big|_{\alpha=1}$ can be rewritten as follows to account for randomness of the seismic response by considering the maximum ductility coefficients to vary within ranges $1-\mu_a$ and $1-\mu_f$, respectively.

$$\zeta'_a\Big|_{\alpha=1} = 0.8\times\frac{1}{\mu_f}\int_1^{\mu_f}\zeta'_a|_{\alpha=1}(\mu)d\mu = \frac{0.4pm\sqrt{1+m^2}}{\eta z\mu_f}\ln\left(\frac{z\mu_f+w}{z+w}\right) \tag{44}$$

$$\zeta'_f\Big|_{\alpha=1} = \frac{1}{\mu_f}\int_1^{\mu_f}\zeta'_f|_{\alpha=1}(\mu)d\mu = \frac{2\rho}{\pi\mu_f}\left\{\ln\left[\frac{(z\mu_f+w)^{\left(1+\frac{w}{z}\right)}}{\mu_f^z}\right] - \left(1+\frac{w}{z}\right)\ln(z+w)\right\}. \tag{45}$$

2.5.3. Elastic–plastic response reduction indexes

Neglecting the inelastic behaviour of the primary structure, R_d and R_a can be defined as evaluation indexes for control effect of the additional system based on ζ_0. When the primary structure operates within the inelastic range, ζ^*_{eq} includes effects of ζ_0 as well as the nonlinear hysteretic damping ratio ζ^*_f. An expression for ζ^*_{eq} can, therefore, be written as

$$\zeta^*_{eq} = \zeta_0 + \zeta^*_f. \tag{46}$$

In accordance with Eq. (13), ζ^*_f with μ_f can be expressed as

$$\zeta^*_f = \frac{2\rho(1-\beta)(\mu_f-1)}{\pi\mu_f(1+\beta\mu_f-\beta)}. \tag{47}$$

Considering that value of the maximum ductility coefficient varies between 1 to μ_f owing to the randomness of seismic response, ζ^*_f can be rewritten as [51]

$$\zeta^*_f = \frac{1}{\mu_f}\int_1^{\mu_f}\zeta^*_f(\mu)d\mu = \frac{2\rho}{\pi\beta\mu_f}\ln\frac{1+\beta\mu_f-\beta}{\mu_f^{\beta}}. \tag{48}$$

In consideration of the inelastic behaviour of the primary structure, R'_d and R'_a can be introduced as elastic–plastic response reduction indexes, and the corresponding $R'_d - R'_a$ curve, thus obtained, is referred to as EPRRC. Values of R'_d and R'_a can, therefore, be calculated using following expressions [51].

(i) For SPS ($0.1\ s < T \leqslant T_g$):

$$R'_d = \frac{S_d(T'_{eq},\zeta'_{eq})}{S_d(T'_f,\zeta^*_{eq})} = \frac{\eta_{2eq'}}{\eta_{2f}}\left(\frac{T'_{eq}}{T'_f}\right)^2 \tag{49}$$

$$R'_a = \frac{\eta_{2eq'}}{\eta_{2f}} \tag{50}$$

where η_{2f} and $\eta_{2eq'}$ denote damping modification factors for ζ^*_{eq} and ζ'_{eq}, respectively.

(ii) For MPS ($T_g < T \leqslant 5\ T_g$):

$$R'_d = \frac{S_d(T'_{eq},\zeta'_{eq})}{S_d(T'_f,\zeta^*_{eq})} = \frac{\eta_{2eq'}}{\eta_{2f}}\left(\frac{T'_{eq}}{T'_f}\right)^{2-\gamma_{2eq'}}\left(\frac{T'_f}{T_g}\right)^{\gamma_{2f}-\gamma_{2eq'}} \tag{51}$$

$$R'_a = \frac{\eta_{2eq'}}{\eta_{2f}}\left(\frac{T'_{eq}}{T'_f}\right)^{-\gamma_{2eq'}}\left(\frac{T'_f}{T_g}\right)^{\gamma_{2f}-\gamma_{2eq'}} \tag{52}$$

where γ_{2f} and $\gamma_{2eq'}$ denote exponential indexes concerning descending branches of ζ^*_{eq} and ζ'_{eq}, respectively.

2.6. Comparison between EPRRC and ERRC

A group of EPRRCs have been plotted in Fig. 9 using Eqs. (49)–(52) by setting parameter values $T_f/T_g = 1.5$, $\alpha = 0.2$, $\beta = 0.6$, and $\rho = 2/3$ (type B in Table 1) with different values of μ_f ($\mu_f = 1.5$, 2.0, and 3) for SPS and MPS. Meanwhile, $\zeta_0 = 0.05$, $0.5 \leqslant p \leqslant 5$, and $0 \leqslant q \leqslant 10$—i.e., identical to their corresponding values considered in the ERRC case plotted in Fig. 5. It must be noted that for SPS, it is unnecessary to set a value of T_f/T_g. Fig. 9, in fact, depicts a comparison between EPRRCs (solid red curves) and corresponding ERRCs (dotted black curves), and demonstrates that the shape of an EPRRC is similar to that of ERRC for both SPS and MPS. That said, there exist differences between the two sets of curves that must be noted for practical applications. To determine the differences between the two curve sets, a displacement reduction ratio φ_d and acceleration reduction ratio φ_a can be introduced such that

$$\varphi_d = \frac{R'_d - R_d}{R_d}\times 100\% \tag{53}$$

$$\varphi_a = \frac{R'_a - R_a}{R_a}\times 100\% \tag{54}$$

Consider a typical curve for each set with parameters $p = 2$ and $q = 1$ and corresponding reduction ratios for SPS and MPS as listed in Tables 2–5. Most values in these tables are positive; however, there exist certain negative values when values of q and μ_f become large for SPS. This implies that under most conditions, ERRC overestimates the effects of vibration control on displacement and acceleration for both SPS and MPS.

Reference to Tables 2 and 3 demonstrates that for $p = 2$, within the

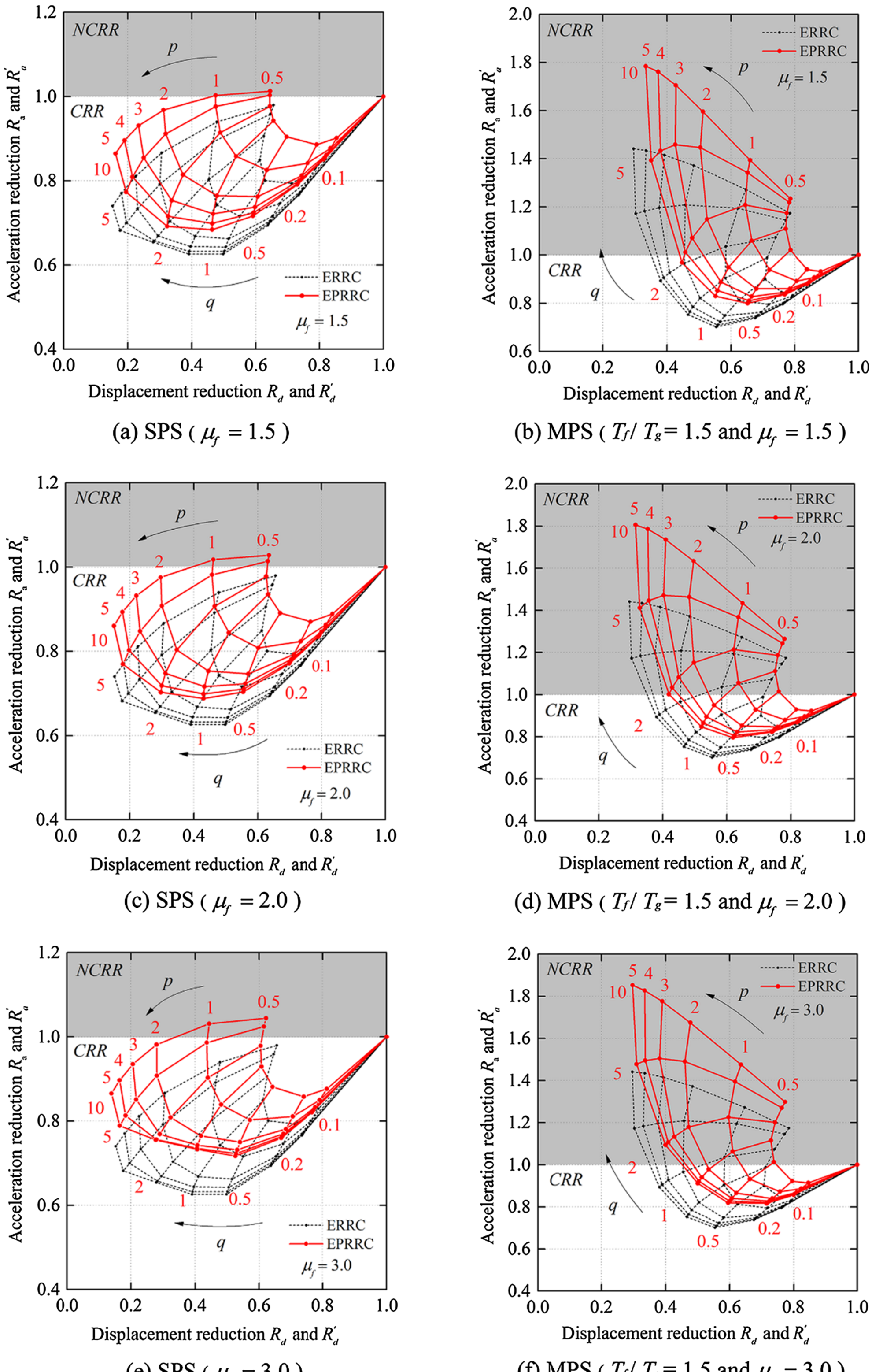

Fig. 9. Comparison between EPRRCs and ERRCs corresponding to conditions (α = 0.2; ζ_0 = 0.05).

given parameter range of q and considering μ_f as constant for both SPS and MPS, increase in the value of q first results in an increase in values of φ_d and φ_a followed by subsequent decrease after attainment of a specific value. This indicates that for constant stiffness of the primary structure, increasing the nominal stiffness of the viscous element first amplifies overestimations in displacement and acceleration, and subsequently, these overestimations start decreasing. Reference to Tables 4 and 5 indicates that for q = 1 and increasing values of p, the value of φ_d increases for the two structures, thereby indicating that under constant stiffness of the primary structure, increasing the stiffness of the equivalent supporting brace amplifies the displacement overestimation. However, the value of φ_a first increases in accordance with

Table 2
Response reduction ratios for SPS ($p = 2$).

Reduction ratio	μ_f	q						
		0.1	0.2	0.5	1	2	5	10
φ_d	1.5	10%	14%	18%	17%	12%	6%	2%
	2.0	7%	9%	11%	9%	5%	0%	−3%
	3.0	4%	5%	5%	2%	−2%	−6%	−8%
φ_a	1.5	10%	13%	15%	14%	16%	15%	12%
	2.0	8%	11%	13%	13%	14%	15%	13%
	3.0	7%	9%	13%	14%	15%	15%	13%

Table 3
Response reduction ratios for MPS ($p = 2$).

Reduction ratio	μ_f	q						
		0.1	0.2	0.5	1	2	5	10
φ_d	1.5	10%	13%	17%	18%	16%	10%	6%
	2.0	7%	9%	12%	11%	9%	6%	3%
	3.0	5%	6%	7%	6%	4%	1%	−1%
φ_a	1.5	10%	13%	15%	16%	19%	20%	16%
	2.0	8%	11%	14%	16%	19%	21%	19%
	3.0	7%	10%	16%	19%	22%	23%	22%

Table 4
Response reduction ratios for SPS ($q = 1$).

Reduction ratio	μ_f	p					
		0.5	1	2	3	5	8
φ_d	1.5	7%	13%	17%	18%	18%	19%
	2.0	3%	6%	9%	9%	10%	10%
	3.0	−1%	1%	2%	3%	4%	5%
φ_a	1.5	11%	16%	14%	12%	10%	9%
	2.0	10%	14%	13%	11%	10%	10%
	3.0	9%	13%	14%	15%	16%	17%

Table 5
Response reduction ratios for MPS ($q = 1$).

Reduction ratio	μ_f	p					
		0.5	1	2	3	5	8
φ_d	1.5	8%	14%	18%	18%	18%	18%
	2.0	5%	9%	11%	12%	12%	12%
	3.0	2%	5%	6%	7%	7%	7%
φ_a	1.5	12%	17%	16%	13%	11%	10%
	2.0	12%	17%	16%	14%	13%	13%
	3.0	13%	18%	19%	20%	21%	21%

that of μ_f, followed by subsequent decrease, and ultimately a continuous increase. This, once again, reflects the overestimation tendency of acceleration under said conditions. In conclusion, reference to Tables 2–5 with $p = 2$ and $q = 1$ demonstrates that when μ_f increases, φ_d decreases, thereby indicating that an increase in ductility of the primary structure tends to enhance the effect of control on displacement. However, under identical conditions, for small values of μ_f, the value of φ_a decreases except for the MPS case with $q = 1$. For large values of μ_f, the value of φ_a continues to increase, thereby indicating that in general, a small ductility of the primary structure enhances the effects of control on acceleration while large ductility tends to weaken the same.

On the other hand, within given parameter ranges, as depicted in Fig. 9, a significant part of the curves is located within CRR of each EPRRC for SPS, whereas for MPS, only a small part of the curves is located within CRR of each EPRRC. Since CRR for SPS is larger compared to that for MPS, it is easier to determine optimum parameter values for SPS compared to MPS. However, increasing the value of μ_f moves EPRRCs towards NCRR, thereby indicating that the preferred region of design parameters becomes small owing to increased ductility of the primary structure.

3. EPRRC-based design procedure

Based on EPRRC, the authors herein have proposed a method for design of a structure equipped with viscous dampers. The operational flowchart of the method is depicted in Fig. 10. Details of the design processes are presented below.

Step 1: Plot the capacity spectrum and calculate storey stiffness of the primary structure. Based on results of pushover analysis of the primary structure, $Q_i - d_i$ relationships between the storey shear force Q_i and storey drift d_i—defined as the maximum storey displacement divided by storey height [55]—must first be obtained. Subsequently, capacity spectrum of the spectral acceleration S_a and spectral displacement S_d can be plotted using the acceleration–displacement response spectrum format [53], also known as the $S_a - S_d$ curve. Next, stiffness K_{fi} of the ith storey of the primary structure can be calculated using the $Q_i - d_i$ relationship as follows.

$$K_{fi} = Q_{ei}/\Delta_{ei} \tag{55}$$

where Q_{ei} and Δ_{ei} denote the ith-storey shear force and displacement, respectively, within the elastic range.

Step 2: Determine the arrangement of viscous dampers. The performance point of the primary structure can be considered as the point of intersection between the demand and capacity spectrum that meets the design displacement requirement [53]. In according with this performance point, the value of the corresponding ith-storey displacement reduction R_{di} can be obtained using

$$R'_{di} = [d]/d_i \tag{56}$$

When R'_{di} is less than 1.0, and viscous dampers should be installed in the corresponding storey to reduce the relatively large drift [56].

Step 3: Obtain the EPRRC. The target storey drift $[d]$ being set in terms of the design requirement; then, the target structural performance point (TSPP) can be determined [57,58]. Subsequently, the capacity spectrum can be represented, based on the bilinear curve, by connecting the origin and TSPP in accordance with the energy equivalent method, and the yielding point (S_{dy}, S_{ay}) can be obtained [57]. Consequently, ductility coefficient μ_f of the primary structure and ratio of the post-yielding stiffness β can be expressed as

$$\mu_f = \frac{S_{dp}S_{ay}}{S_{dy}S_{ap}} \tag{57}$$

$$\beta = \frac{(S_{ap} - S_{ay})S_{dy}}{(S_{dp} - S_{dy})S_{ay}}. \tag{58}$$

The fundamental period ratio T_1/T_g can be obtained via modal analysis of the primary structure, and the value relative velocity exponent α can be set in accordance with required specifications of viscous dampers. Upon determination of these parameters, the corresponding EPRRC can, subsequently, be obtained.

Step 4: Calculate the parameters of viscous dampers. The nominal viscous element stiffness ratio $q_i = K'_{di}/K_{fi}$ can be determined for the ith storey using EPRRC in accordance with the determined value of R_{di} and setting the equivalent supporting-brace stiffness ratio to $p_i = K^*_{bi}/K_{fi}$. Subsequently, the ith nominal stiffness of the viscous element K'_{di} can be determined. Considering the relationship between maximum displacement of the structure equipped with viscous dampers $u_{i,\max}$ and that of viscous dampers $u_{di,\max}$ for the ith storey, the maximum damping force $F_{di,\max}$, described in detail in Appendix A, can be determined using the relation

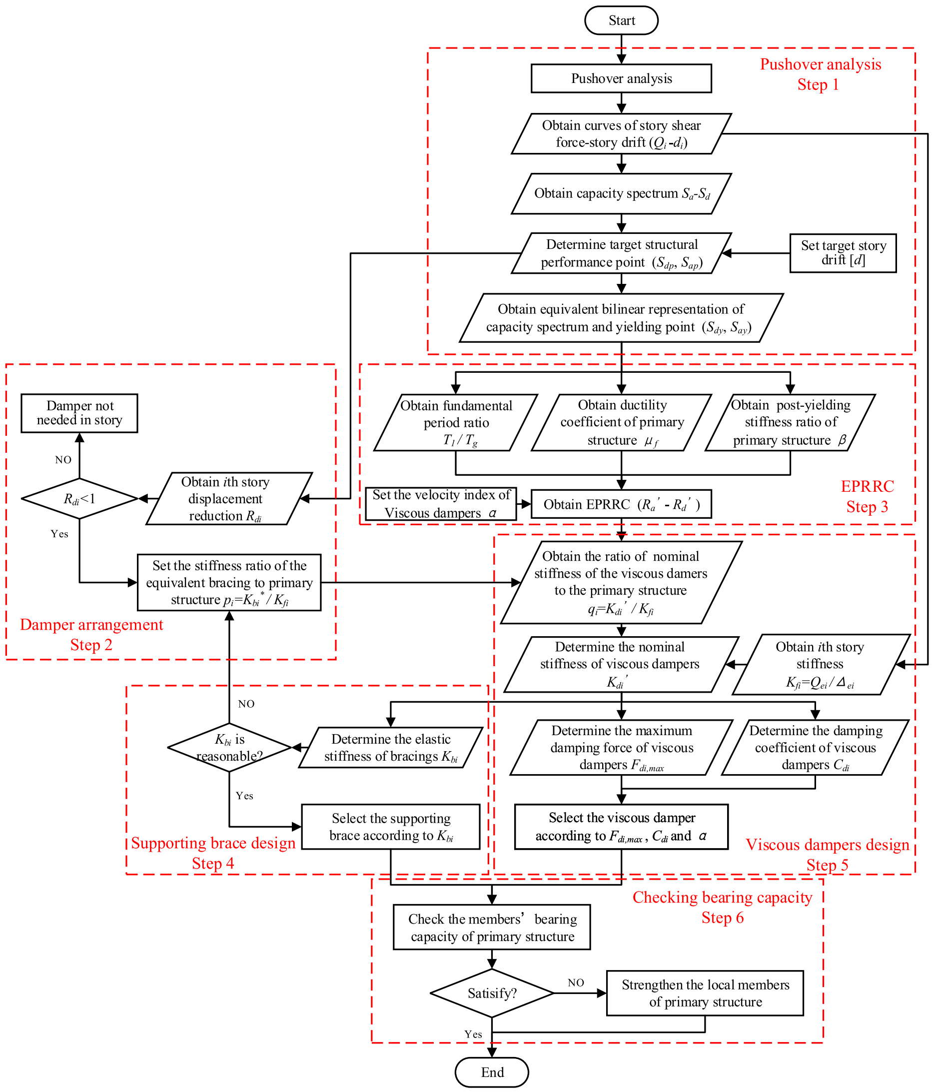

Fig. 10. Design flowchart for structures equipped with viscous dampers.

$$F_{di,\max} = \frac{u_{i,\max} K'_{di}}{[1 + (1/m_i)^{1+\alpha}]^{1-0.5\alpha}}. \tag{59}$$

In accordance with Eq. (3), the damping coefficient C_{di} of viscous dampers on the ith storey can be expressed as

$$C_{di} = K'_{di} u_{i,\max}^{1-\alpha} \left(\frac{T'_{i,eq}}{2\pi}\right)^{\alpha} \left(\frac{u_{di,\max}}{u_{i,\max}}\right)^{1-\alpha} \tag{60}$$

$$T'_{i,eq} = T_1 \sqrt{\frac{1 + \beta\mu_f - \beta}{1 + \beta\mu_f - \beta + \frac{p}{1 + m_i^{1+\alpha}}\mu_f}}. \tag{61}$$

Upon determination of above parameters, the selection of viscous dampers can be proceeded with.

Step 5: Select a section of the supporting brace. For series connection between viscous elements and supporting braces, the stiffness K_{bi} of supporting braces on the ith storey can be calculated using the following relation.

$$K_{bi} = \frac{(K_{di}/K_{fi})(K^*_{bi}/K_{fi})}{(K_{di}/K_{fi}) - (K^*_{bi}/K_{fi})} = \frac{p_i (K_{di}/K_{fi})}{(K_{di}/K_{fi}) - p_i} \tag{62}$$

where $K_{di} = \chi C_{di}$ and χ denotes the internal stiffness coefficient [2]. However, a reasonable value of K_{bi} must be considered in practice. The design can be proceeded to the next step after appropriate selection of the supporting brace. Else, the designer might be required to repeat steps 4 and 5.

Step 6: The bearing capacity of members of the primary structure must be checked. This step involves comparison of local forces using time-history analysis and local bearing capacity of members of the primary structure connected to viscous dampers. If design requirements pertaining to said members are satisfied, the design process can be terminated; else, local members must be strengthened prior to termination of the design process.

4. Example

4.1. Model information

In this study, the proposed design method was applied to a ten-storey steel frame benchmark structure introduced in [2]. The plan and elevation profiles of the steel frame are depicted in Fig. 11, and square steel tubular column and H-profile steel beam sections in all storeys are listed in Tables 6 and 7. The equivalent thicknesses of concrete slab reinforced by U-profile steel are all 125 mm in floors and roof. Under seismic excitation, floor dead and live loads are 5.95 kN/m^2 and 0.8 kN/m^2, respectively, and the roof dead and live loads are 8.79 kN/m^2 and 0.6 kN/m^2, respectively. Table 8 lists the mass of each storey and the inherent damping ratio ζ_0 of the structure is 0.02.

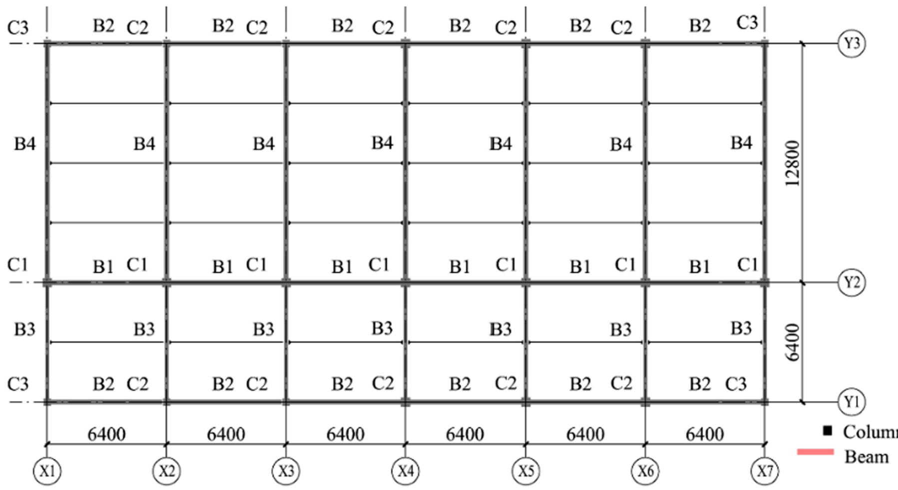

(a) Plan of steel frame

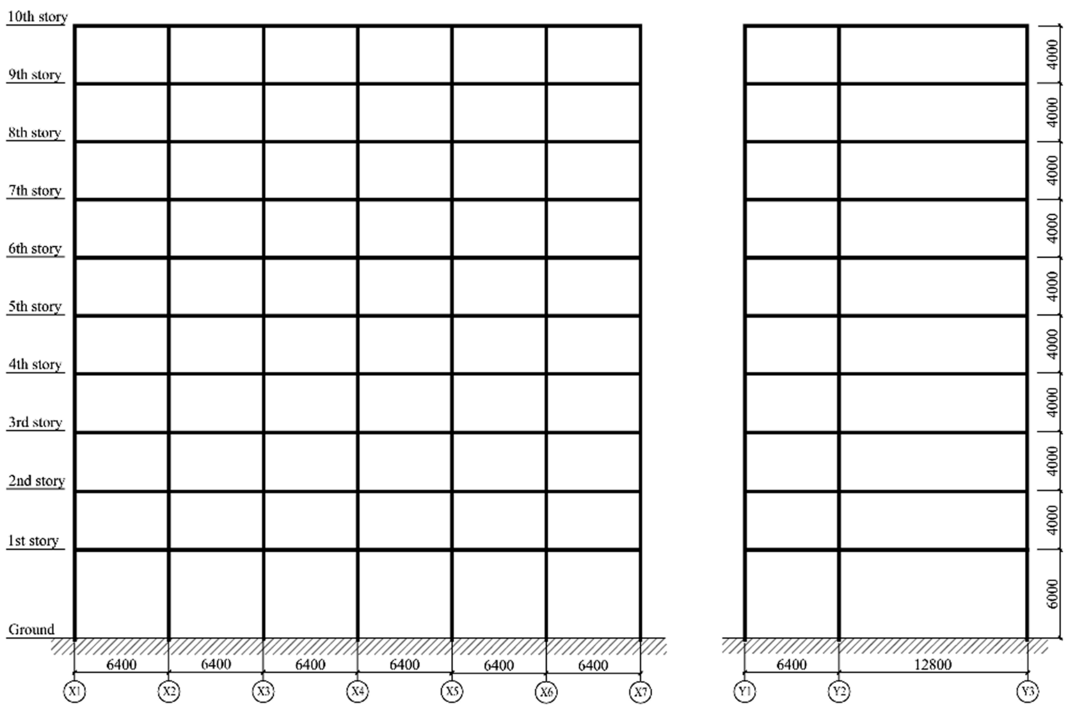

(b) Elevation of steel frame

Fig. 11. Plan and elevation of benchmark model.

Table 6
Column sections.

Sectional number of column		C1	C2	C3
Storey	1	500 × 500 × 36[a]	450 × 450 × 36	450 × 450 × 28
	2	500 × 500 × 28	450 × 450 × 25	450 × 450 × 19
	3	500 × 500 × 28	450 × 450 × 25	450 × 450 × 19
	4	450 × 450 × 28	450 × 450 × 25	400 × 400 × 19
	5–6	450 × 450 × 25	400 × 400 × 25	400 × 400 × 19
	7	400 × 400 × 28	350 × 350 × 28	350 × 350 × 16
	8	400 × 400 × 25	350 × 350 × 25	350 × 350 × 16
	9–10	350 × 350 × 25	350 × 350 × 25	350 × 350 × 16

[a] Note: 500 × 500 × 36 is 500 mm × 500 mm × 36 mm (width × width × thickness).

This ten-storey steel frame is modelled as a three-dimensional nonlinear model. A regular symmetrical trilinear stress–strain relationship were adopted from the Perform3D software to model the steel material [59]. The yielding stress of the structural steel is 335 MPa for all beams and columns, and the corresponding nonlinear parameters of this material can be determined from Chinese code for design of steel structure [60]. Beams and columns were modelled as elastic rods with inelastic regions located at both ends. Plastic hinges and fibre segments were used for the beams and columns, respectively. A trilinear model of the moment–curvature type was adopted for plastic hinges in Perform3D [52,59]. In this study, the equivalent shear wave velocity of soil equalled 240 m/s while the covered soil thickness equalled 28 m. Based on site conditions T_g equalled 0.4 s [55]. The models with and without viscous dampers are denoted as ST0 and ST1, respectively. The first

Table 7
Beam sections.

Sectional number of beam		B1	B2	B3	B4
Storey	2	500 × 350 × 16 × 32[a]	500 × 300 × 16 × 28	500 × 350 × 16 × 36	500 × 350 × 16 × 36
	3	500 × 350 × 16 × 28	500 × 350 × 16 × 25	500 × 350 × 16 × 32	500 × 350 × 16 × 36
	4	500 × 350 × 16 × 28	500 × 350 × 16 × 25	500 × 350 × 16 × 32	500 × 350 × 16 × 36
	5	500 × 350 × 16 × 25	500 × 350 × 16 × 25	500 × 350 × 16 × 28	500 × 350 × 16 × 36
	6	500 × 350 × 12 × 22	500 × 300 × 12 × 22	500 × 350 × 16 × 28	500 × 350 × 16 × 32
	7	500 × 350 × 12 × 22	500 × 300 × 12 × 22	500 × 350 × 12 × 25	500 × 350 × 12 × 32
	8	500 × 350 × 12 × 19	500 × 300 × 12 × 19	500 × 300 × 12 × 25	500 × 300 × 16 × 32
	9	500 × 300 × 12 × 19	500 × 300 × 9 × 16	500 × 300 × 12 × 25	500 × 300 × 16 × 32
	10	450 × 300 × 9 × 16	450 × 200 × 12 × 19	450 × 300 × 12 × 19	450 × 300 × 16 × 28
	Roof	450 × 200 × 9 × 16	450 × 200 × 9 × 12	450 × 300 × 16 × 28	450 × 350 × 16 × 32

[a] Note: 500 × 350 × 16 × 32 is 500 mm × 350 mm × 16 mm × 32 mm (height × width × web thickness × flange thickness).

Table 8
Model information.

Storey	Storey height (m)	Mass of storey m_i (t)	Total mass of story Σm_i (t)
10	4	842.1	842.1
9	4	602.3	1444.4
8	4	609.5	2053.9
7	4	614.0	2667.9
6	4	620.8	3288.7
5	4	622.8	3911.5
4	4	628.9	4540.4
3	4	635.7	5176.1
2	4	635.7	5811.8
1	6	667.1	6478.9

three modal periods are listed in Table 9 from the modal analysis of ST0.

4.2. Damper arrangement and design process

Upon completion of the pushover analysis for ST0, the corresponding capacity spectrum was obtained. In accordance with performance requirements [2], the target storey drift [d] was limited to within 1/150 for a peak ground acceleration (PGA) of 0.4 g. The yielding point (169.7 mm, 176.3 Gal) was determined after evaluating TSPP (207.3 mm, 192.3 Gal) for PGA = 0.4 g. Calculated values of the post-yielding stiffness ratio β and ductility coefficient μ_f equalled 0.41 and 1.12, respectively. The storey elastic stiffness values of ST0 were determined according to the pushover analysis and listed in Table 10.

The storey drifts d_i for ST0 were determined based on the TSPP, whereas the displacement-reduction ratio R'_{di} was determined based on [d] and d_i, as listed in Table 11. Based on the result obtained for R'_{di}, it was observed that $R'_{di} < 1$ from the 1st-7th stories, and therefore, viscous dampers must be installed on these floors. In the said design, viscous dampers were installed as diagonal members with an inclined angle of φ_i within the primary structure whilst being simultaneously located at the beam–column centreline joint, as depicted in Fig. 12.

Because the first modal period for ST0 $T_1 = 1.934$ s lied between $T_g = 0.4$ s and $5T_g = 2$ s, ST0 could be considered as MPS. By setting $\alpha = 0.2$, $\mu_f = 1.12$, $\beta = 0.41$, and $T_1/T_g = 4.83$, EPRRC was plotted, as depicted in Fig. 13. In accordance with R'_{di} and CRR for EPRRC, the stiffness ratio was assumed to be $p_i = 1.5$ for the 1st and 2nd storeys, $p_i = 1.0$ for the 4th and 5th storeys and $p_i = 0.5$ for other storeys. The expected corresponding nominal stiffness ratios q_i were directly read from EPRRC, as listed in Table 12. Subsequently, for $\chi = 7\ \mathrm{cm}^{-0.8}\cdot\mathrm{s}^{-0.2}$, storey-design parameters concerning viscous dampers and supporting braces were obtained, and the same have been listed in Table 11. Each storey was symmetrically equipped with six viscous dampers, as depicted in the plan view in Fig. 12, and supporting braces made of profile steel were adopted. Calculated parameters and standard specifications for both viscous dampers and supporting braces are listed in Table 13.

4.3. Bearing-capacity analysis

4.3.1. Seismic input

Two artificial (AW1 and AW2) and twenty natural (NW1–NW20) seismic waves were selected in this study based on the Chinese design response spectrum with characteristic period T_g of 0.4 s, and the corresponding normalized design spectrum could be expressed as

$$S_{pa} = \begin{cases} 1 + 11.5T, & (0 \ < T \leqslant 0.1\mathrm{s}) \\ 2.25, & (0.1\ \mathrm{s}< T \leqslant 0.4\mathrm{s}) \\ 2.25\left(\frac{0.4}{T}\right)^{0.9}, & (0.4\ \mathrm{s}< T \leqslant 2\mathrm{s}) \\ 2.25[0.2^{0.9} - 0.02(T-2)], & (0.2\ \mathrm{s}< T \leqslant 6\mathrm{s}) \end{cases} \tag{63}$$

Corresponding normalized response spectra, the average spectrum, and target spectrum are all depicted in Fig. 14. Details concerning these natural waves are listed in Table 14. All natural seismic waves were selected from the strong motion database of the Pacific Earthquake Research Centre [61].

For time-history analysis, 12 waves—AW1, AW2, and NW1–NW10—were considered out of the above-mentioned 22. Prior to performing the time-history analysis, all seismic waves were adjusted by a scale factor in accordance with the Chinese code for different intensities—frequent, moderate, and severe—of seismic events with target PGA = 0.14 g, 0.4 g, and 0.62 g, respectively [55,62]. Subsequently, IDA was performed using 20 natural waves (NW1–NW20).

4.3.2. Internal force comparisons of local structure

Based on the design results described in section 4.2, viscous dampers were to be installed on storeys 1–7. To compare the internal forces within members of the ST0 and ST1 configurations, the said non-linear time-history analysis was performed considering the same 12 seismic waves as mentioned earlier. All non-linear time-history analyses were

Table 9
Modal periods for ST0.

Modals	1st modal	2nd modal	3rd modal
Period (s)	1.934	0.771	0.447

Table 10
Elastic stiffness distribution for ST0.

Storey	1	2	3	4	5	6	7	8	9	10
Elastic stiffness K_{fi} (kN/cm)	2691	3788	3886	3253	3017	2901	2419	2192	1843	1624

performed using the direct integration algorithm with combination of 1% modal damping and 1% Rayleigh damping in the Perform3D software [52]. Local structures should be used to analyse internal forces of the local members connected directly to the dampers. Considering the longitudinal symmetry of the structure, the local structures 1, 2 and 3, shown in Fig. 12, are selected in storeys 1–7 along with Y1, Y2 and Y3 directions between X2 and X3, respectively. In order to identify the specific member of local structures, a subscript is attached to the sectional number, which is used in Fig. 11(a), Tables 6 and 7, as Cx_{ijk} and Bx_{ij} for column and beam, respectively, where x denotes sectional number, i denotes local structure number from 1 to 3, j denotes storey number from 1 to 7 and k denotes axis number from 2 to 3. For example, $C1_{112}$ represents that column $C1$ locates at the 1st storey of local structure 1 along axis 2, and $B1_{11}$ represents that beam $B1$ locates at the 1st storey of local structure 1. In each local structure, fourteen columns and seven beams are directly connected to viscous dampers, as depicted in Fig. 12. Usually, for columns, internal forces corresponding to the maximum moment $M_{\max}$, maximum shear force $V_{\max}$, and maximum axial force $P_{\max}$ must be checked, on the other hand, for beams $M_{\max}$ and $V_{\max}$ are considered to be checked. Upon completion of the time-history analysis under PGA = 0.14 g, 0.4 g, and 0.62 g, maximum average internal forces of sections were calculated and listed in Table 15. To quantify differences between these maximum average internal forces of sections corresponding to ST0 and ST1, a comparison index was defined as follows.

$$\Gamma = \frac{F_{ST1} - F_{ST0}}{F_{ST0}} \times 100\% \tag{64}$$

Here, F_{ST0} and F_{ST1} denote maximum average internal forces of section for ST0 and ST1, respectively.

Reference to Table 15 demonstrates that the comparison index Γ corresponding to $P_{\max}$ of columns within the local structure are positive, whereas all other values of Γ are negative. This implies that $P_{\max}$ of columns tends to increase while all other internal forces within columns and beams decrease upon installation of viscous dampers under conditions of identical seismic excitation. It is, therefore, necessary to check the bearing capacity of columns to ensure the safety of structure.

4.3.3. Bearing-capacity check for local structure

The bearing-capacity check of profile steel columns commonly includes section strength check and overall stability check. Under ultimate state, the bearing-capacity of steel member should satisfy the following expressions according to Chinese code for design of steel structure [60].

(i) For frequent seismic exercitation

$$S \leqslant R/\gamma_{RE} \tag{65}$$

where S denotes load effect, R denotes design resistance calculated by design strength f of steel and γ_{RE} denotes the modification factor of seismic resistance, which is set to 0.75 and 0.80 for strength and stability checks of steel column [55], respectively, to mainly consider the increase of material strength under seismic exercitation.

(ii) For moderate seismic exercitation

$$S \leqslant R_k \tag{66}$$

where R_k denotes the nominal resistance calculated by the yielding strength f_y of steel.

For severe seismic exercitation, however, only structural deformation is required to be checked according to Chinese code for seismic design of buildings [55], which is presented in the following section. To guarantee the safety of energy dissipation structure, the Eq. (66) was also applied under severe seismic exercitation.

In frequent seismic event, the section strength of steel column can be checked by [60]

$$\frac{N_{cs}}{A_n} \pm \frac{M_{cs}}{\gamma_x W_n} \leqslant f \tag{67}$$

where N_{cs} and M_{cs} are axial force and moment of column section, respectively; A_n and W_n are net area and modulus of column section, respectively; γ_x is plastic development coefficient. However, under moderate and severe seismic exercitations, f_y should be used instead of f to check the section strength of steel column.

On the other hand, the overall stability of steel column can be checked using following equations [60].

$$\frac{N_{cm}}{\varphi_x A} + \frac{\beta_{mx} M_{cm}}{\gamma_x W_{1x}\left(1 - 0.8\frac{N_{cm}}{N'_{Ex}}\right)} \leqslant f \tag{68}$$

$$N'_{Ex} = \frac{\pi^2 EA}{1.1\lambda_x^2} \tag{69}$$

where N_{cm} and M_{cm} are maximum axial force and moment of steel

Table 11
Pushover analysis results for ST0.

Storey	1	2	3	4	5	6	7	8	9	10
Shear force (pushover) Q_i (kN)	11,012	10,733	10,350	9649	8834	7996	6671	5341	3864	2270
Storey drift (pushover) d_i (m/m)	1/117	1/119	1/137	1/127	1/133	1/140	1/141	1/164	1/191	1/286
Target storey drift [d] (m/m)	1/150									
Reduction ratio of displacementR'_{di}	0.77	0.79	0.91	0.84	0.88	0.93	0.93	1.08	1.26	1.89
Storeys requiring dampers	1, 2, 3, 4, 5, 6, 7									

column within computational range, respectively; A and W_{1x} are gross area and modulus of section, respectively; λ_x is slenderness ratio; φ_x is stability coefficient of axial compressive member and β_m is equivalent moment coefficient.

In accordance with Chinese code for design of steel structure [60], f and f_y are 295 MPa and 335 MPa, respectively, in this study. Determined by Eqs. (67)–(69), critical axial force and moment curves and the maximum combinations of the column axial force and moment under conditions of PGA = 0.14 g, 0.4 g, and 0.62 g have been respectively plotted in Figs. 15 and 16 for section strength and overall

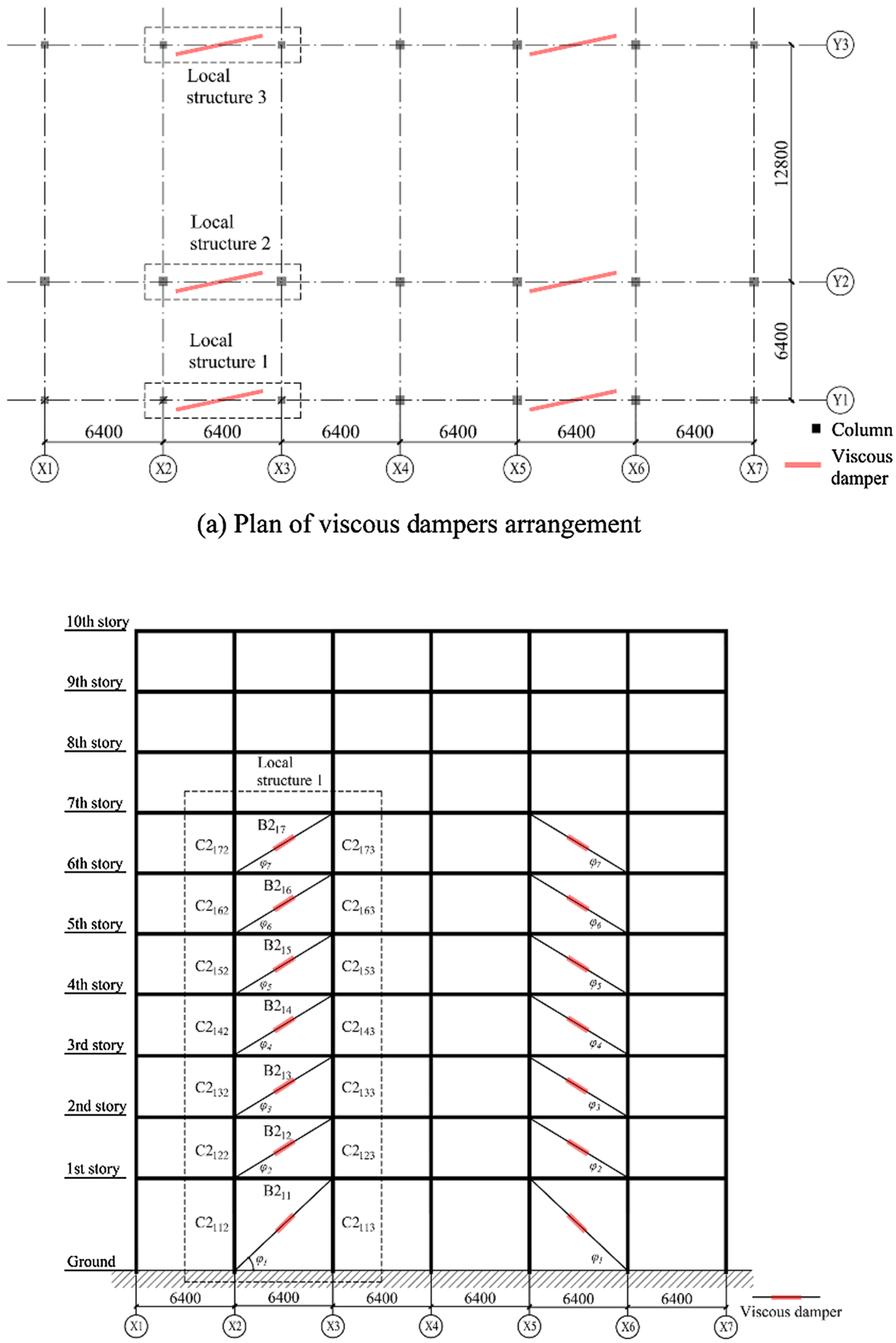

(a) Plan of viscous dampers arrangement

(b) Elevation of viscous dampers arrangement in Y1

Fig. 12. Plan and elevation of viscous-damper arrangement.

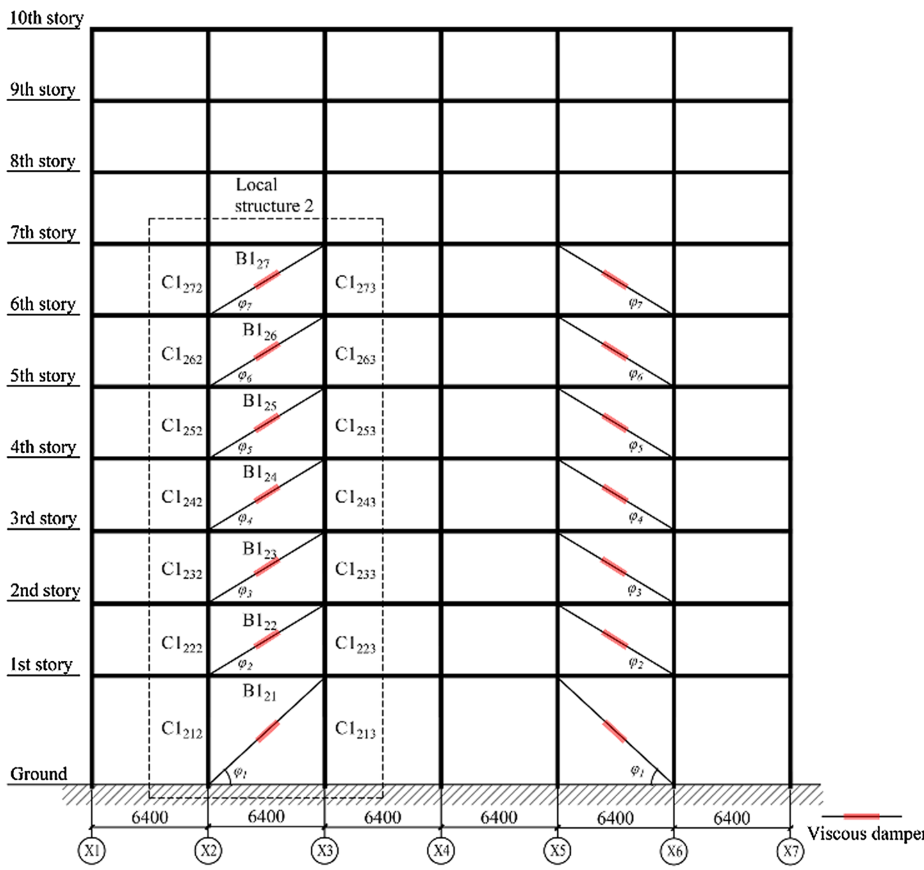

(c) Elevation of viscous dampers arrangement in Y2

Fig. 12. (*continued*)

stability. The said figures demonstrate that all points of internal force combinations are located within the corresponding axial force and moment curve, thereby implying that the bearing capacity of these columns can well satisfy force combinations. If the bearing capacity of columns fails to meet the requirement of the internal force combinations, corresponding columns must be strengthened to guarantee structural safety.

4.4. Verification of mitigation effect

To investigate differences in structural response between elastic and inelastic primary structures equipped with viscous dampers, performance of a primary elastic structure with the same installed viscous damper denoted as ST2 was compared against ST1. To investigate differences in the vibration effect for configurations ST0, ST1, and ST2, a non-linear time history analysis was performed under the 12 different seismic waves, as described in Section 4.3.1. Values of average storey drifts and shear forces corresponding to configurations ST0, ST1, and ST2 were compared using results obtained via analysis and plotted in Figs. 17–19. These figures indicate that viscous dampers in ST1 can effectively control storey drifts within 1/250, 1/150, and 1/80 in the event of frequent, moderate, and severe seismic activities, respectively. The average shear force of ST1 at each storey was observed to be effectively reduced upon installation of viscous dampers. Therefore, average storey drifts and shear forces were observed to have been effectively reduced at the same time, and superiority of CRR was observed in the design of structures equipped with viscous dampers.

Because primary structures corresponding to both ST1 and ST2 configurations lied almost within the elastic range under frequent seismic activity, ST2 demonstrate attainment of a nearly identical vibration-control effect as ST1 for both cases of average storey drift and shear force. In the event of moderate and severe seismic activities, however, average storey drifts for ST2 were observed to be larger compared to those of ST1, and the average shear force for ST2 significantly exceeded that of ST0. This demonstrates that inelastic behaviour of the primary structure plays an important role in vibration control, especially when the primary structure operates within the inelastic range.

Maximum values of storey drifts and shear forces for the ST0 and ST1 configurations are listed in Table 16 corresponding to different

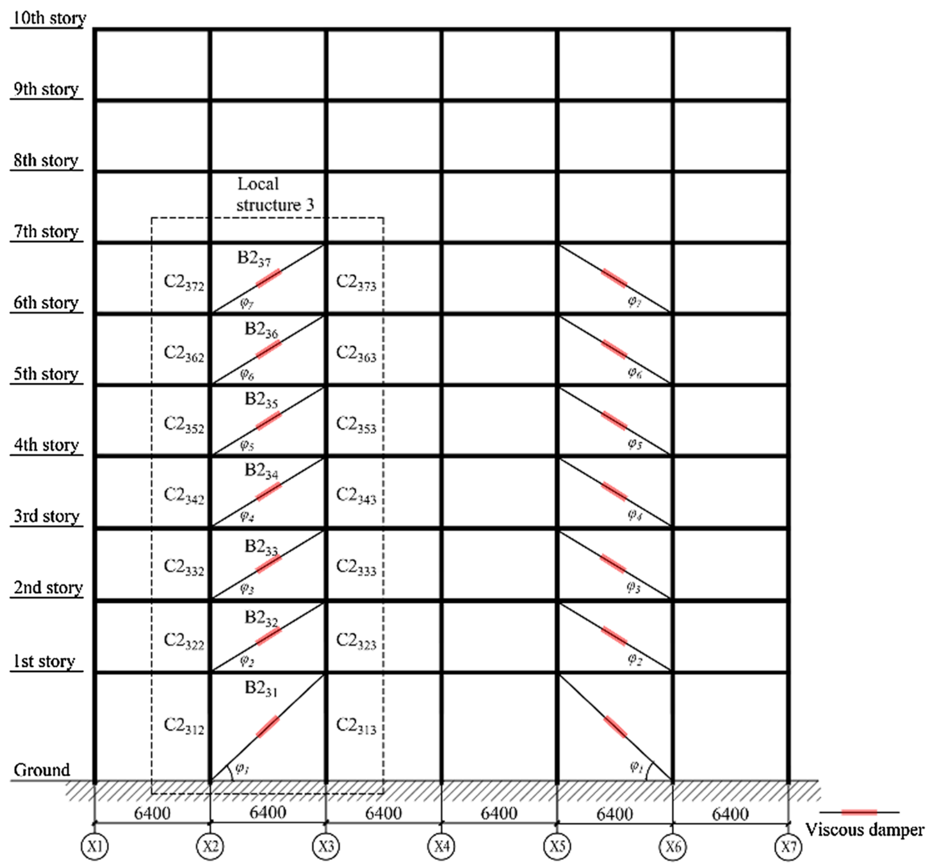

(d) Elevation of viscous dampers arrangement in Y3

Fig. 12. (*continued*)

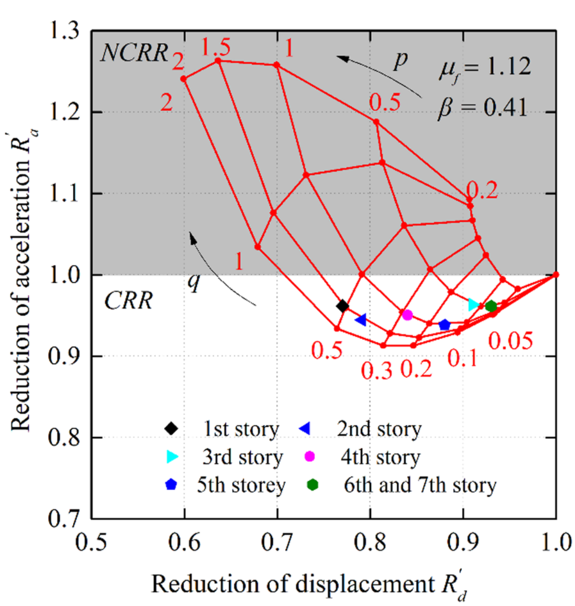

Fig. 13. Storey demand points in EPRRC ($\alpha = 0.2$; $T_1/T_g = 4.83$).

PGAs of seismic waves. To quantify the vibration control effect, a comparison index has been introduced as follows.

$$\kappa = \frac{R_{ST0} - R_{ST1}}{R_{ST1}} \times 100\% \tag{70}$$

In the above equation, R_{ST0} and R_{ST1} denote maximum seismic responses for ST0 and ST1, respectively. Compared to ST0, both the maximum storey drift and maximum storey force for ST1 were observed to be effectively mitigated, especially in the event of the moderate seismic activity with PGA = 0.4 g, as described in Table 16. Therefore, results of non-linear time-history analysis demonstrate the effectiveness of the proposed design method.

In order to quantify the energy dissipation of viscous dampers, the comparisons of energy dissipation between the structure with and without viscous dampers under PGA = 0.14, 0.4 and 0.62 g of natural seismic wave NW1 have been conducted, and the results shown in Figs. 20–22. From these figures, the energy percentages clearly indicate that the installed viscous dampers can dissipate sufficient seismic energy under different intensities of seismic events and effectively reduce the dissipated inelastic energy especially with the higher intensity.

Table 12
Design parameters of viscous dampers and supporting braces at each storey.

Storey	1	2	3	4	5	6	7
Stiffness ratio p_i	1.50	1.50	0.50	1.00	1.00	0.50	0.50
Nominal stiffness ratio q_i	0.5118	0.4202	0.1231	0.2790	0.1508	0.0751	0.0751
Nominal stiffness K'_{di}(kN/cm)	1377.25	1591.72	478.37	907.59	454.96	217.87	181.67
Maximum damping force $F_{di,\max}$(kN)	4426.50	3560.86	1095.45	2031.96	1111.90	532.66	444.16
Damping coefficient C_{di}(kN·s$^{0.2}$·cm$^{-0.2}$)	2674.77	2322.79	725.68	1337.50	724.83	349.42	291.36
Supporting brace stiffness K_{bi}(kN/cm)	5145.88	8733.84	3146.54	4985.05	7442.42	3564.09	2971.92
Inclined anglecos φ_i	0.7295	0.8480	0.8480	0.8480	0.8480	0.8480	0.8480
Axial maximum damping force $F'_{di,\max}$(kN)	6067.55	4199.14	1291.80	2396.19	1311.20	628.14	523.77
Axial damping coefficient C'_{di}(kN·s$^{0.2}$·cm$^{-0.2}$)	3905.08	2831.21	884.45	1630.12	883.41	425.87	355.11

Table 13
Calculated parameters and standard specifications for each viscous damper and supporting brace.

Storey		1	2	3	4	5	6	7
Number of viscous dampers		6	6	6	6	6	6	6
Calculated parameters of each viscous damper	Axial maximum damping force $F'_{di,\max}$(kN)	1011.25	699.86	215.30	399.36	218.53	104.69	87.30
	Axial damping coefficient C'_{di}(kN·s$^{0.2}$·cm$^{-0.2}$)	650.85	471.87	147.41	271.69	147.24	70.98	59.18
Standard specifications for the parameters of each viscous damper	Length L_d (cm)	100	100	100	100	100	100	100
	Maximum damping force F_d (kN)	1050	700	250	400	250	150	100
	Damping coefficient C_d (kN·s$^{0.2}$·cm$^{-0.2}$)	650	500	150	300	150	100	60
Calculated parameters of each supporting brace	Length L_{bi} (cm)	877	755	755	755	755	755	755
	Elastic stiffness E_{bi} (kN/cm)	20,600	20,600	20,600	20,600	20,600	20,600	20,600
	Cross-sectional area (cm^2)	32.36	46.26	16.67	26.41	39.42	18.88	15.74
Profile steel parameters of each supporting brace[a]	Specification of profile steel	HM 250 × 175						
	Cross-sectional area A_p (cm^2)	56.24						

[a] Note: The specifications and parameters of profile steel were selected and determined from the Chinese standard for hot-roll H and cut T section steel (GB/T 11263–1998).

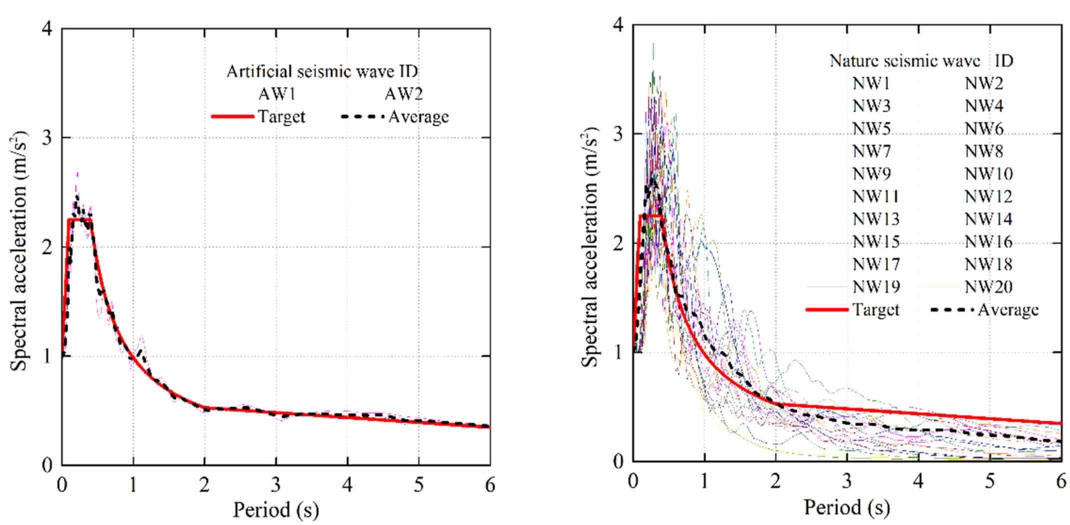

(a) Artificial seismic waves AW1 and AW2 (b) Natural seismic waves NW1 - NW20

Fig. 14. Normalized response spectra of artificial and natural seismic waves.

Table 14
Details of natural waves.

ID	RSN	Year	Magnitude	$\bar{v}_s$ (m/s)	Epicentral distance (km)	Event	Station
NW1	9	1942	6.5	213.44	56.88	Borrego	El Centro Array #9
NW2	12	1952	7.36	316.46	114.62	Kern County	LA-Hollywood Stor FF
NW3	26	1961	5.6	198.77	19.55	Hollister-01	Hollister City Hall
NW4	68	1971	6.61	316.46	22.77	San Fernando	LA-Hollywood Stor FF
NW5	93	1971	6.61	298.68	39.45	San Fernando	Whittier Narrows Dam
NW6	131	1976	5.91	249.28	41.37	Friuli_Italy-02	Codroipo
NW7	138	1978	7.35	324.57	24.07	Tabas Iran	Boshrooyeh
NW8	154	1979	5.74	335.5	19.46	Coyote Lak	San Juan Bautista_24 Polk S
NW9	163	1979	6.53	205.78	23.17	Imperial Valley-06	Calipatria Fire Statio
NW10	169	1979	6.53	242.05	22.03	Imperial Valley-06	Delta
NW11	186	1979	6.53	212	35.64	Imperial Valley-06	Niland Fire Station
NW12	218	1980	5.42	304.68	29.31	Livermore-02	Antioch-510 G St
NW13	229	1980	5.19	329	18.39	Anza (Horse Canyon)-01	Rancho De Anza
NW14	268	1980	6.33	259.59	39.1	Victoria_Mexico	SAHOP Casa Flores
NW15	287	1980	6.9	356.39	44.62	Irpinia Italy-01	Bovino
NW16	307	1981	5.9	309.41	25.31	Taiwan MART1(5)	SMART1 I0
NW17	312	1981	5.9	314.33	23.77	Taiwan MART1(5)	SMART1 O07
NW18	316	1981	5.9	348.69	16.54	Westmorland	Parachute Test Site
NW19	322	1983	6.36	274.73	23.78	Coalinga-01	Cantua Creek School
NW20	328	1983	6.36	230.57	44.82	Coalinga-01	Parkfield-Cholame 3 W

4.5. Incremental dynamic analysis

In addition to the above-described non-linear time-history analysis, a more rigorous probabilistic framework was employed in this study to further validate the proposed design method and quantify the likelihood of having the response of a retrofitted system exceed admissible limits. To this end, an IDA was performed on the ST0 and ST1 configurations. During IDA, all 20 natural seismic waves listed in Table 14 were considered. To match the Chinese seismic code, values of PGA and maximum storey drift $\theta_{\max}$ were considered to be indicative of the intensity and damage measures of IDA, respectively. Resulting IDA curves are depicted in Fig. 23, wherein limits of the maximum storey drift are denoted as $\theta_{\max} = 1/250$, 1/150, and 1/80 corresponding to the frequent, moderate, and severe seismic activities.

In Fig. 23, an obvious dispersion can be observed among values of the maximum storey drift under identical PGAs for different seismic waves. For the ST0 configuration featured in Fig. 23(a), most waves can be observed to intersect the intensity level by exceeding the corresponding drift limit, which cannot be considered safe. On the other hand, for the ST1 case, depicted in Fig. 23(b), most waves were observed to intersect the intensity level without exceeding the corresponding drift limit. This result indicates that installation of viscous dampers enhances primary-structure performance in a significant way, thereby demonstrating effectiveness of the proposed design methodology.

To qualify the exceedance probability of the structure before and after retrofit, a fragility analysis was adopted as a probabilistic methodology based on the IDA curves generated in the above exercise. Lognormal curves obtained via least-square minimization were used to generate fragility curves. The median fragility capacity $IM_{c,50}$—defined as the 50th fractile of a lognormal fragility curve—and logarithmic standard deviation β_c were considered two parameters concerning fragility curves related to one another via the following relation.

$$\beta_c = \frac{1}{2}\ln\left(\frac{IM_{c,84}}{IM_{c,16}}\right) \tag{71}$$

Here, $IM_{c,84}$ and $IM_{c,16}$ denote intensity-measure values corresponding to the 84th and 16th fractile of a lognormal fragility curve, respectively [63].

Fragility curves corresponding to maximum storey drifts of $\theta_{\max} = 1/250$, 1/150, and 1/80 for configurations ST0 (dotted curve) and ST1 (solid line) are plotted in Fig. 24. The comparison between cases ST1 and ST0, as depicted in Fig. 24, demonstrates exceedance probabilities P_f for $\theta_{\max} = 1/250$, 1/150, and 1/80 to have significantly decreased from 28%, 92%, and 70% to 0, 35%, and 5% under PGA values of 0.14 g, 0.40 g, and 0.62 g, respectively. It can, therefore, be stated that reliability of the proposed design has been demonstrated in the view of a realm of a rigorous probabilistic framework.

5. Conclusions

The proposed study presents an elastic–plastic method based on EPRRC for design of a structure equipped with viscous dampers. The proposed method accounts for inelastic behaviour of the primary structure, and traditional ERRCs have been extended to EPRRCs through use of viscous damper. EPRRCs and ERRCs were analysed and compared. A detailed design procedure was formulated in the form of a flowchart, and a ten-storey steel frame benchmark model was used to illustrate the design process. A non-linear time-history analysis and IDA

Table 15
Comparison between maximum average internal forces of sections within local structures subjected to PGA = 0.14 g, 0.4 g, and 0.62 g.

Section (Number)	Internal force	PGA = 0.14 g			PGA = 0.4 g			PGA = 0.62 g		
		ST0	ST1	Γ	ST0	ST1	Γ	ST0	ST1	Γ
500 × 500 × 36 ($C1_{212}$, $C1_{213}$)	M_{max}[a]	1568	429	−72.6%	2035	1212	−40.4%	2075	1748	−15.8%
	P_{max}[b]	5281	6243	18.2%	5362	6689	24.7%	5439	7257	33.4%
	V_{max}[c]	564	169	−70.0%	657	445	−32.3%	693	627	−9.5%
500 × 500 × 28 ($C1_{222}$,$C1_{232}$,$C1_{223}$,$C1_{233}$)	M_{max}	1218	654	−46.3%	1645	1321	−19.7%	1660	1574	−5.2%
	P_{max}	4229	4566	8.0%	4323	4693	8.6%	4381	4818	10.0%
	V_{max}	574	323	−43.7%	777	638	−17.9%	797	739	−7.3%
450 × 450 × 36 ($C2_{112}$,$C2_{113}$,$C2_{312}$,$C2_{313}$)	M_{max}	1188	317	−73.3%	1868	868	−53.5%	1902	1348	−29.1%
	P_{max}	3301	4227	28.1%	3335	4670	40.0%	3323	4823	45.1%
	V_{max}	440	122	−72.3%	594	320	−46.1%	601	499	−17.0%
450 × 450 × 28 ($C1_{242}$,$C1_{243}$)	M_{max}	1088	565	−48.1%	1358	1179	−13.2%	1426	1304	−8.6%
	P_{max}	3708	3979	7.3%	3782	4096	8.3%	3862	4136	7.1%
	V_{max}	522	275	−47.3%	661	570	−13.8%	713	656	−8.0%
450 × 450 × 25 ($C2_{122}$, $C2_{132}$, $C2_{123}$, $C2_{133}$, $C2_{322}$, $C2_{332}$, $C2_{323}$, $C2_{333}$, $C1_{252}$, $C1_{262}$, $C1_{253}$, $C1_{263}$)	M_{max}	924	611	−33.9%	1317	1213	−7.9%	1360	1315	−3.3%
	P_{max}	2687	2714	1.0%	2757	2772	0.5%	2800	2816	0.6%
	V_{max}	442	296	−33.0%	637	587	−7.8%	665	660	−0.8%
400 × 400 × 28 ($C1_{272}$, $C1_{273}$)	M_{max}	843	560	−33.6%	1207	1158	−4.1%	1258	1231	−2.1%
	P_{max}	2185	2193	0.4%	2228	2229	0.0%	2256	2258	0.1%
	V_{max}	407	271	−33.4%	587	563	−4.1%	624	602	−3.5%
400 × 400 × 25 ($C2_{142}$, $C2_{152}$,$C2_{162}$, $C2_{143}$, $C2_{153}$, $C2_{163}$, $C2_{342}$, $C2_{352}$, $C2_{362}$, $C2_{343}$, $C2_{353}$, $C2_{363}$)	M_{max}	648	426	−34.3%	1063	856	−19.5%	1178	1126	−4.4%
	P_{max}	1688	1714	1.5%	1699	1779	4.7%	1695	1804	6.4%
	V_{max}	311	206	−33.8%	498	415	−16.7%	562	517	−8.0%
350 × 350 × 28 ($C2_{172}$, $C2_{173}$, $C2_{372}$, $C2_{373}$)	M_{max}	564	373	−33.9%	956	780	−18.4%	996	973	−2.3%
	P_{max}	1364	1376	0.9%	1373	1416	3.1%	1376	1437	4.4%
	V_{max}	272	180	−33.8%	462	379	−18.0%	476	473	−0.6%
500 × 300 × 16 × 28 ($B2_{11}$, $B2_{31}$)	M_{max}	877	238	−72.9%	1138	667	−41.4%	1139	1093	−4.0%
	V_{max}	251	88	−64.9%	356	202	−43.3%	361	281	−22.2%
500 × 350 × 16 × 25 ($B2_{12}$, $B2_{13}$, $B2_{32}$, $B2_{33}$)	M_{max}	787	294	−62.6%	1149	710	−38.2%	1154	1141	−1.1%
	V_{max}	233	104	−55.4%	364	209	−42.6%	367	288	−21.5%
500 × 300 × 16 × 25 ($B2_{14}$, $B2_{34}$)	M_{max}	601	276	−54.1%	1004	687	−31.6%	1018	1001	−1.7%
	V_{max}	202	104	−48.5%	314	194	−38.2%	321	296	−7.8%
500 × 300 × 12 × 22 ($B2_{15}$, $B2_{16}$, $B2_{35}$, $B2_{36}$)	M_{max}	549	279	−49.2%	874	702	−19.7%	887	878	−1.0%
	V_{max}	184	106	−42.4%	278	196	−29.5%	284	277	−2.5%
500 × 300 × 12 × 19 ($B2_{17}$, $B2_{37}$)	M_{max}	441	272	−38.3%	771	655	−15.0%	788	780	−1.0%
	V_{max}	147	92	−37.4%	247	176	−28.7%	250	244	−2.4%
500 × 350 × 16 × 32 ($B1_{21}$)	M_{max}	1314	365	−72.2%	1436	1013	−29.5%	1442	1388	−3.7%
	V_{max}	378	132	−65.1%	451	306	−32.2%	459	439	−4.4%
500 × 350 × 16 × 28 ($B1_{22}$, $B1_{23}$)	M_{max}	975	433	−55.6%	1250	1003	−19.8%	1262	1252	−0.8%
	V_{max}	299	153	−48.8%	397	274	−31.0%	398	395	−0.8%
500 × 350 × 16 × 25 ($B1_{24}$)	M_{max}	862	404	−53.1%	1147	990	−13.7%	1164	1148	−1.4%
	V_{max}	287	148	−48.4%	364	277	−23.9%	365	360	−1.4%
500 × 350 × 12 × 22 ($B1_{25}$, $B1_{26}$)	M_{max}	731	412	−43.6%	993	988	−0.5%	1003	1005	0.2%
	V_{max}	241	147	−39.0%	317	274	−13.6%	321	316	−1.6%
500 × 350 × 12 × 19 ($B1_{27}$)	M_{max}	629	393	−37.5%	885	882	−0.3%	891	889	−0.2%
	V_{max}	207	129	−37.7%	283	260	−8.1%	286	281	−1.7%

Note:
[a] M_{max} denotes the maximum moment of member and its unit is kN·m.
[b] P_{max} denotes the maximum axial force of member and its unit is kN.
[c] V_{max} denotes the maximum shear force of member and its unit is kN.

were performed to verify the effectiveness of the proposed method. The main conclusions drawn from this study could be summarized as under.

(i). EPRRCs reflect the relationship between characteristic parameters of viscous dampers, stiffness of the supporting brace, and response of the primary structure with viscous damper by accounting for inelastic behaviour of the primary structure. Therefore, EPRRCs are suitable for use in the design of a structure with viscous

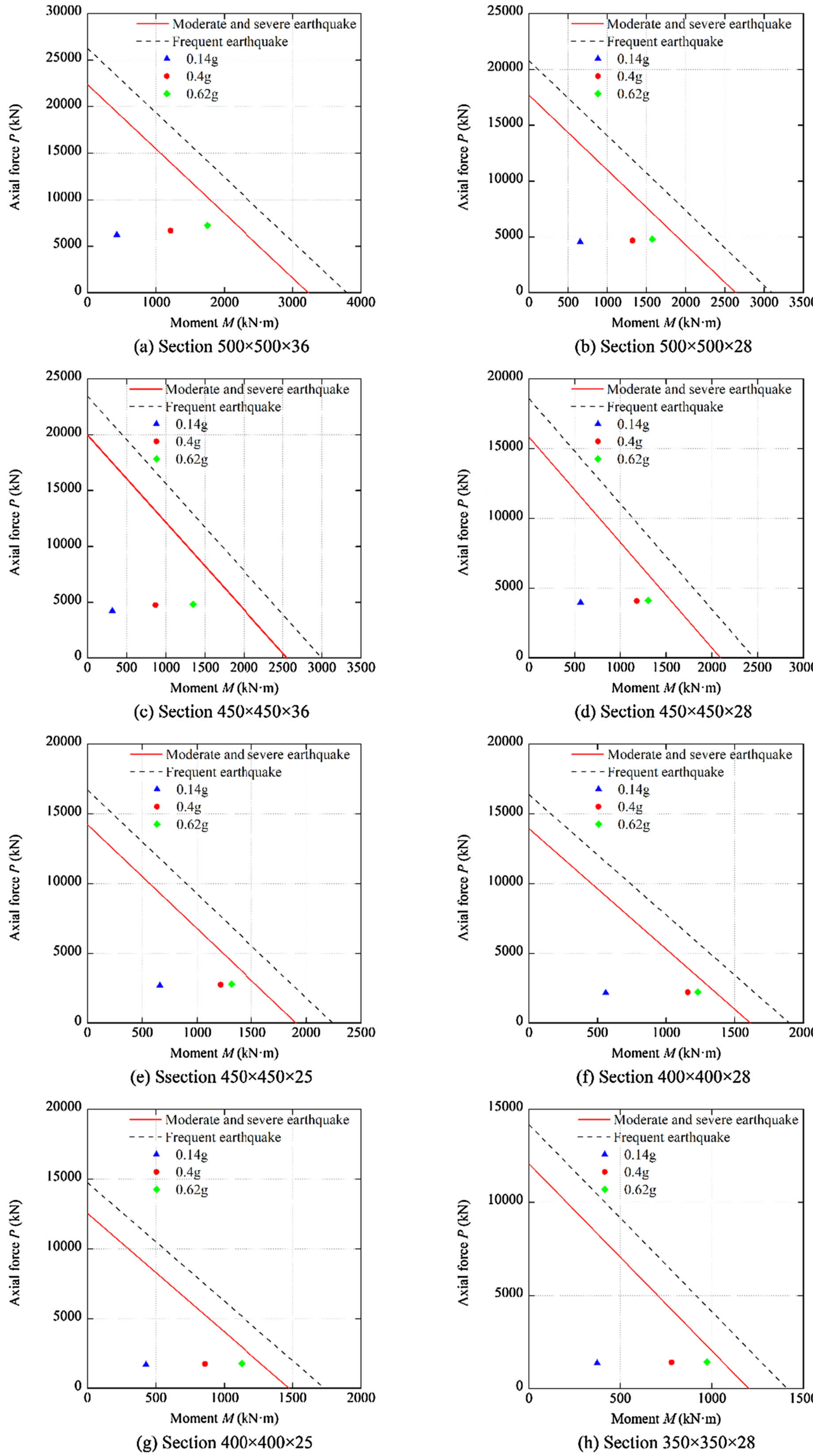

Fig. 15. Axial force and moment curves as well as section strength check for column.

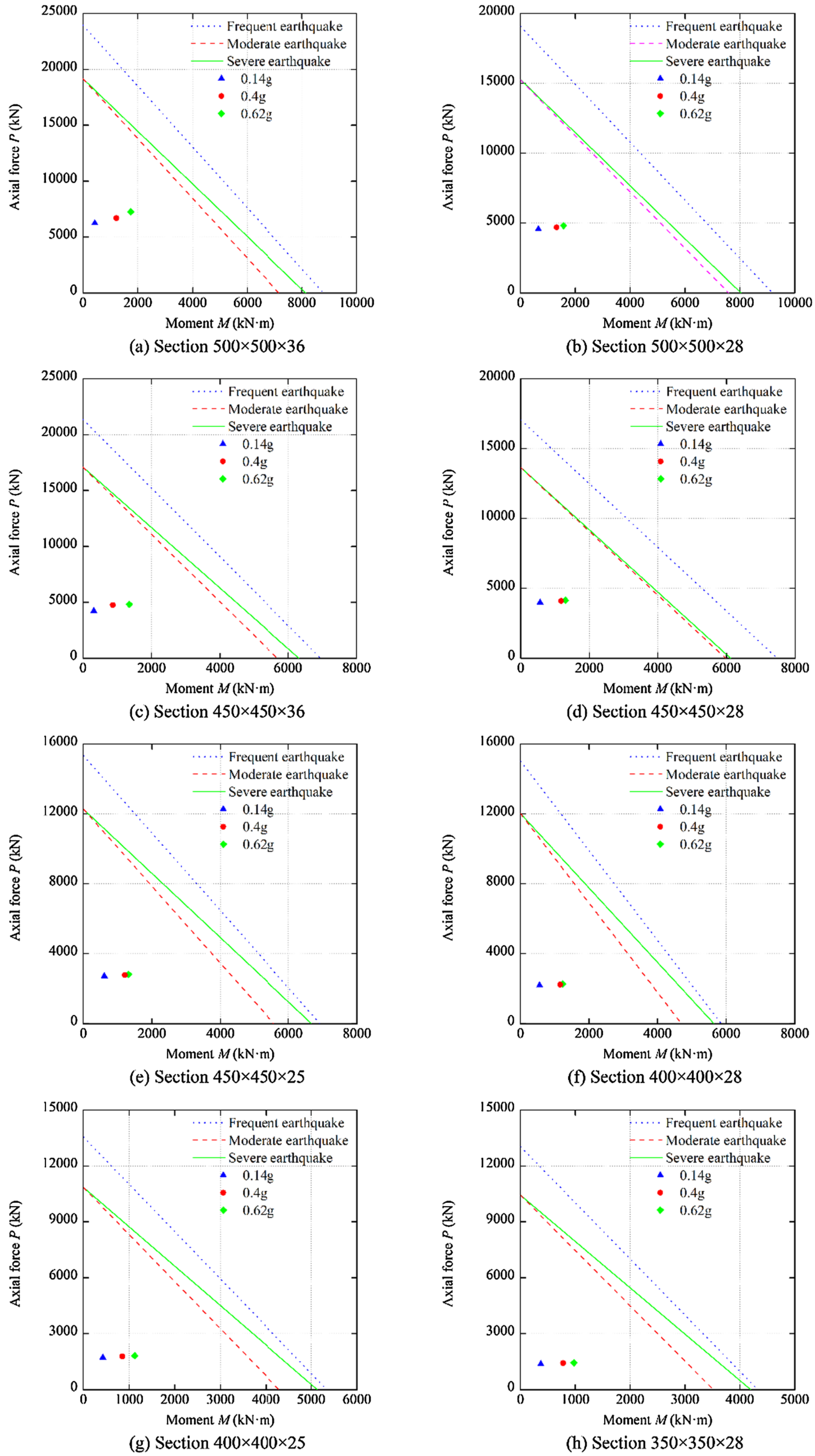

Fig. 16. Axial force and moment curves as well as overall stability check for column.

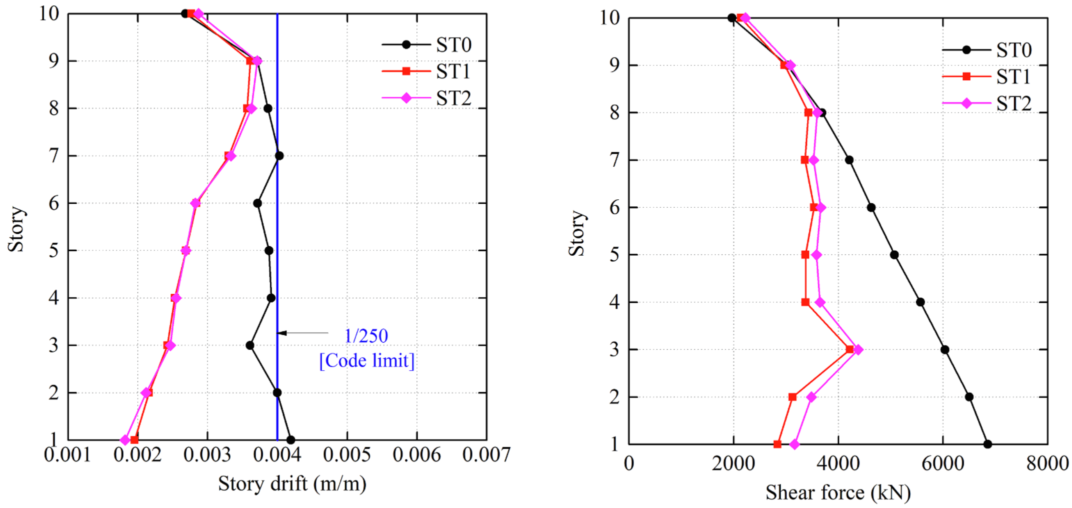

(a) Distribution of average story drifts (b) Distribution of average shear forces

Fig. 17. Average storey drifts and shear forces (PGA = 0.14 g).

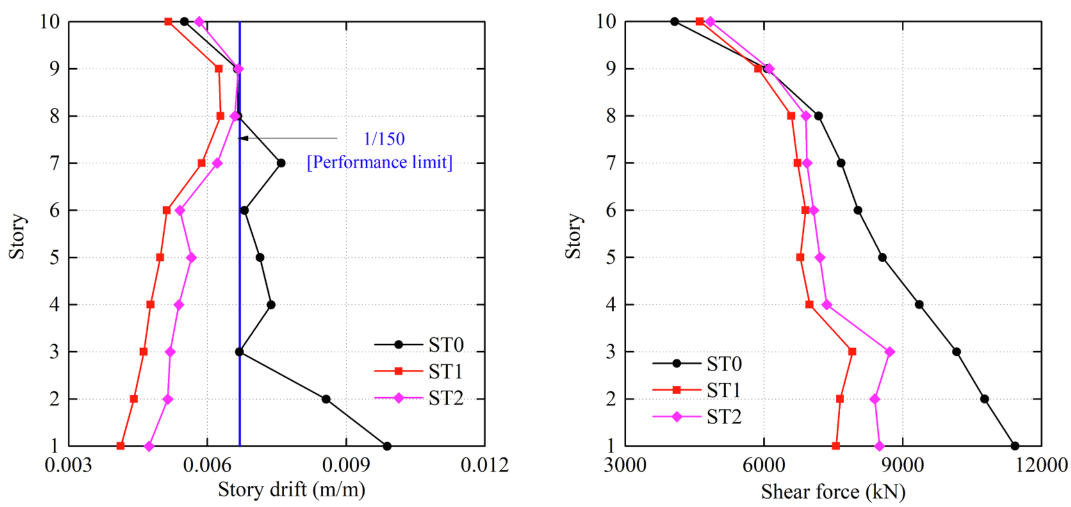

(a) Distribution of average story drifts (b) Distribution of average shear forces

Fig. 18. Average storey drifts and shear forces (PGA = 0.4 g).

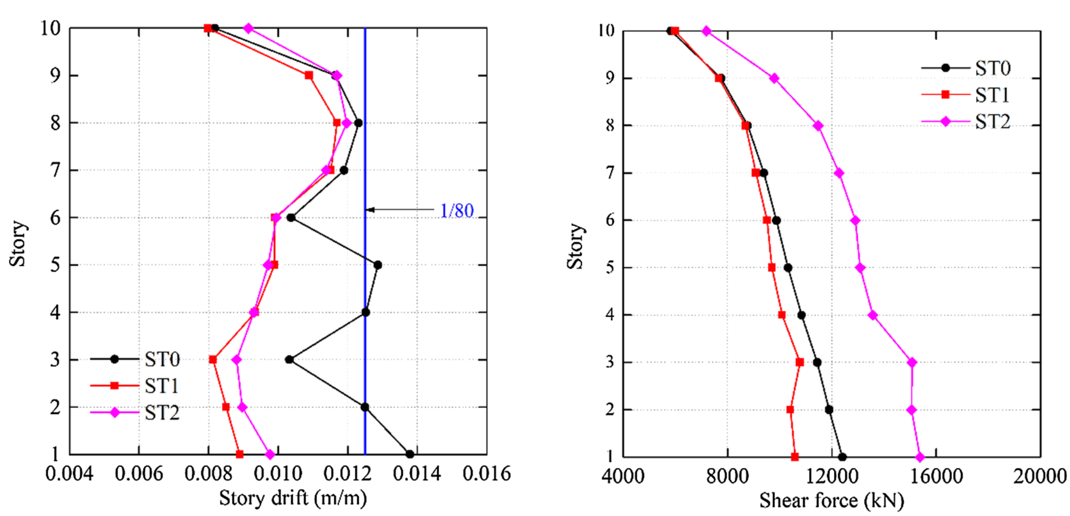

(a) Distribution of average story drifts (b) Distribution of average shear forces

Fig. 19. Average storey drifts and shear forces (PGA = 0.62 g).

Table 16
Comparison index for maximum seismic responses of ST0 and ST1.

Maximum seismic response	PGA (g)	ST0	ST1	Comparison index $\varkappa$
Storey drift (m/m)	0.14	1/239	1/277	16%
	0.4	1/101	1/159	57%
	0.62	1/73	1/84	18%
Storey shear force (kN)	0.14	6856	4220	62%
	0.4	11,426	7913	44%
	0.62	12,402	10,776	15%

dampers and subjected to high-intensity seismic events.

(ii). When the primary structure enters the inelastic range of operation, traditional ERRCs tend to overestimate the effects of vibration control on both displacement and acceleration of the structure equipped with viscous dampers. In contrast, EPRRCs provides a more accurate estimation of the effects of vibration control, thereby ensuring greater safety of the structure.

(iii). Expected reduction points can be achieved in CRR of EPRRC, thereby indicating effective reduction of both the displacement and acceleration of a structure equipped with viscous dampers. Further, it was verified that the proposed design method

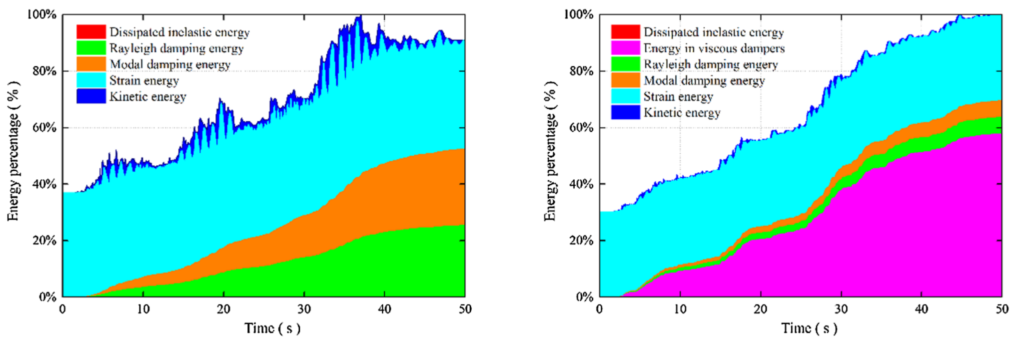

(a) Energy dissipation time history of ST0 under NW1 (PGA = 0.14 g) (b) Energy dissipation time history of ST1 under NW1 (PGA = 0.14 g)

Fig. 20. Energy-dissipation time history for ST0 and ST1 under NW1 (PGA = 0.14 g).

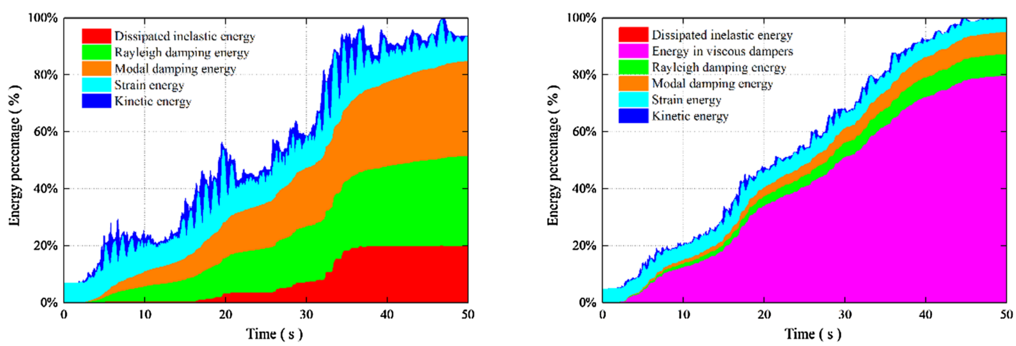

(a) Energy dissipation time history of ST0 under NW1 (PGA = 0.4 g) (b) Energy dissipation time history of ST1 under NW1 (PGA = 0.4 g)

Fig. 21. Energy-dissipation time history for ST0 and ST1 under NW1 (PGA = 0.4 g).

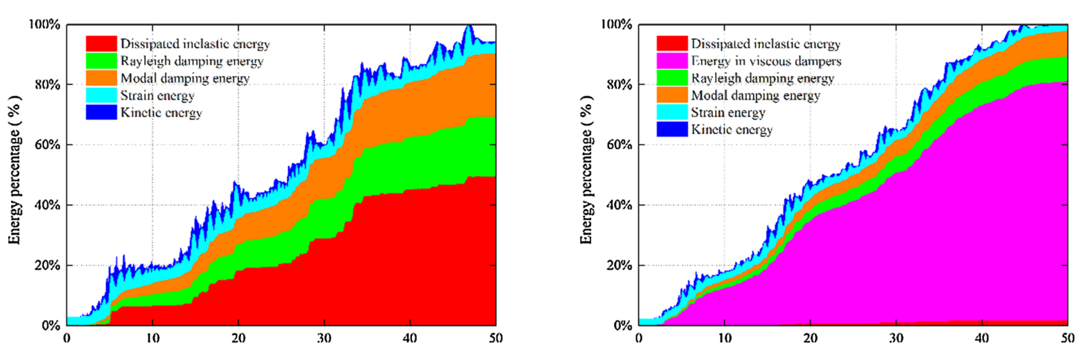

(a) Energy dissipation time history of ST0 under NW1 (PGA = 0.62 g) (b) Energy dissipation time history of ST1 under NW1 (PGA = 0.62 g)

Fig. 22. Energy-dissipation time history for ST0 and ST1 under NW1 (PGA = 0.62 g).

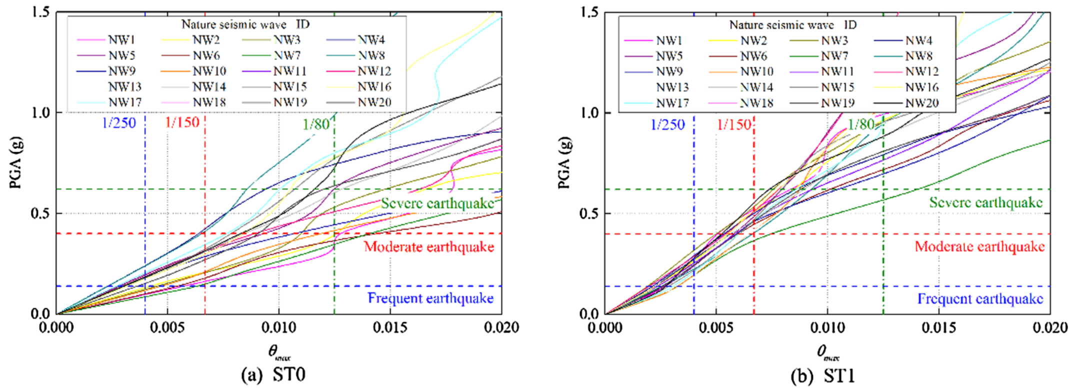

Fig. 23. IDA curves for ST0 and ST1.

effectively satisfies design requirements under the action of different seismic intensities.

Declaration of Competing Interest

The authors declared that there is no conflict of interest.

Acknowledgments

This study was supported by the Nantong Department of Science and Technology, China (Grant No. MS12018053), the National Natural Science Foundation of China (Grant No. 51978525); and the Fundamental Research Funds for the Central Universities, China (Grant No. 22120180064).

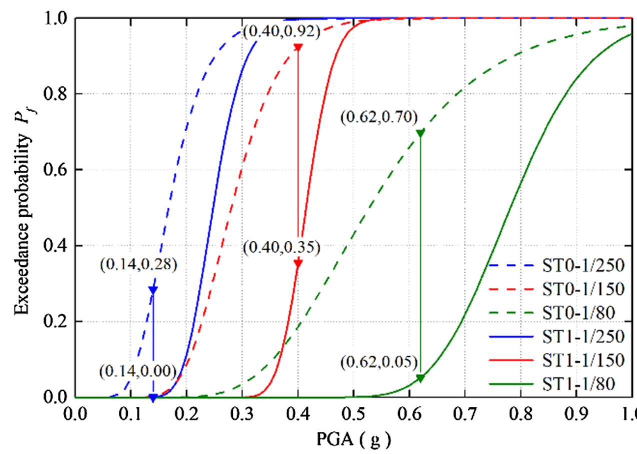

Fig. 24. Fragility curves for ST0 and ST1.

Appendix A. Calculation of maximum damping force $F_{di,\max}$ and stiffness of additional system K_a

Under harmonic excitation, displacement u_d and velocity v_d of the viscous damper can be expressed as

$$u_d = u_{d,\max}\sin\omega t \tag{72}$$

$$v_d = \omega u_{d,\max}\cos\omega t \tag{73}$$

where $u_{d,\max}$ denotes maximum displacement of the viscous damper while ω and t represent the circular frequency and time of the harmonic excitation, respectively. Damping force F_d of the viscous damper could be expressed as

$$F_d = C_d v_d{}^{\alpha} = C_d\omega^{\alpha}u_{d,\max}^{\alpha}(\cos\omega t)^{\alpha} \tag{74}$$

where C_d denotes the damping coefficient and α denotes the relative-velocity exponent.

Since the maximum value of $\cos\omega t$ equals unity, the maximum damping force $F_{d,\max}$ can be expressed as

$$F_{d,\max} = C_d\omega^{\alpha}u_{d,\max}^{\alpha}. \tag{75}$$

Further, nominal stiffness K_d' of the viscous element can be obtained using the relation

$$K_d' = \frac{F_{d,\max}}{u_{d,\max}} = \frac{C_d\omega^{\alpha}u_{d,\max}^{\alpha}}{u_{d,\max}} = \frac{C_d\omega^{\alpha}}{u_{d,\max}^{1-\alpha}}. \tag{76}$$

For series connection, the force F_b^* corresponding to the equivalent supporting brace equals F_d; thus, displacement u_b^* of the equivalent bracing can be expressed as

$$u_b^* = \frac{F_b^*}{K_b^*} = \frac{F_d}{K_b^*} = \frac{C_d\omega^{\alpha}u_{d,\max}^{\alpha}}{K_b^*}(\cos\omega t)^{\alpha} \tag{77}$$

where K_b^* denotes the stiffness of the equivalent supporting brace.

Combining Eqs. (72), (76) and (77) displacement u_a of the additional system can be calculated using the following relation.

$$u_a = u_d + u_b^* = u_d + F_d/K_b^* = u_{d,\max}\left[\sin\omega t + \frac{K_d'}{K_b^*}(\cos\omega t)^{\alpha}\right]. \tag{78}$$

Maximum displacement $u_{a,\max}$ ($\alpha = 0, 1$) of the additional system can be expressed as

$$u_{a,\max} = u_{d,\max}[1 + K_d'/K_b^*]\ (\alpha = 0), \tag{79}$$

$$u_{a,\max} = u_{d,\max}[1 + (K_d'/K_b^*)^2]^{1/2}\ (\alpha = 1). \tag{80}$$

Therefore, $u_{a,\max}$ ($0 \leqslant \alpha \leqslant 1$) can be calculated using the following relation.

$$u_{a,\max} = u_{d,\max}\left[1 + \left(\frac{K_d'}{K_b^*}\right)^{1+\alpha}\right]^{1-0.5\alpha} \tag{81}$$

Supposing that maximum displacement $u_{\max}$ of the primary structure with viscous damper equals $u_{a,\max}$, the maximum damping force $F_{d,\max}$ of the viscous damper can be calculated using the following relation.

$$F_{d,\max} = \frac{u_{\max}K_d'}{[1 + (1/m)^{1+\alpha}]^{1-0.5\alpha}}, \tag{82}$$

$$m = K_b^*/K_d'. \tag{83}$$

Further, stiffness K_a ($\alpha = 0, 1$) of the additional system can be derived as follows.

(i) For $\alpha = 0$, and considering series connection between the viscous element and equivalent supporting brace (Fig. 3(a)), the following equations exist.

$$F_a = F_d = F_b^* \tag{84}$$

$$u_a = u_d + u_b^* \tag{85}$$

where F_a denotes force of the additional system.

Combining Eqs. (84), (85) and $F_b^* = K_b^* u_b^*$, F_d can be expressed as follows.

$$F_d = K_b^*(u_a - u_d). \tag{86}$$

Combining Eqs. (72), (79), (86) F_a can be expressed as

$$F_a = K_b^*[u_{d,\max}(1 + K_d'/K_b^*) - u_{d,max}\sin\omega t]. \tag{87}$$

Using Eq. (84), when $\sin\omega t = 1$, the maximum force $F_{a,\max}$ of the additional system can be expressed as

$$F_{a,\max} = K_b^* u_{d,\max}(K_d'/K_b^*). \tag{88}$$

Therefore, for $\alpha = 0$, K_a can be expressed as

$$K_a = \frac{F_{a,\max}}{u_{a,\max}} = K_b^*\frac{K_d'/K_b^*}{1 + K_d'/K_b^*} = K_b^*\frac{1}{1+m}. \tag{89}$$

(ii) For $\alpha = 1$, Eq. (86) exists, as depicted in Fig. 4(a). Combining Eqs. (72), (80), (86), F_a can be expressed as

$$F_a = K_b^*\{u_{d,\max}[1 + (K_d'/K_b^*)^2]^{1/2} - u_{d,max}\sin\omega t\}. \tag{90}$$

When $\sin\omega t = 1/[1 + (K_d'/K_b^*)^2]^{1/2}$, $F_{a,\max}$ can be expressed as

$$\begin{aligned} F_{a,\max} &= K_b^*\left\{u_{d,\max}\sqrt{1 + (K_d'/K_b^*)^2} - u_{d,max}\frac{1}{\sqrt{1 + (K_d'/K_b^*)^2}}\right\} \\ &= K_b^* u_{d,\max}\frac{(K_d'/K_b^*)^2}{\sqrt{1 + (K_d'/K_b^*)^2}} \end{aligned} \tag{91}$$

Therefore, for $\alpha = 1$, K_a can be expressed as

$$K_a = \frac{F_d}{u_{a,\max}} = K_b^*\frac{(K_d'/K_b^*)^2}{1 + (K_d'/K_b^*)^2} = K_b^*\frac{1}{1+m^2} \tag{92}$$

Appendix B. Calculation of non-linear hysteretic damping ratio for $\alpha = 0$ and $\alpha = 1$

When the primary structure enters the inelastic range, the equivalent damping ratio ζ_{eq} of the inelastic analytical model forms an essential parameter to derive EPRRC. In this study, equivalent damping ratios for cases corresponding to $\alpha = 0$ and $\alpha = 1$ can be derived as under.

1. For $\alpha = 0$, $\zeta_{eq}|_{\alpha=0}$ can be expressed as

$$\zeta_{eq}'|_{\alpha=0} = \zeta_0 + \zeta_a'|_{\alpha=0} + \zeta_f'|_{\alpha=0}. \tag{93}$$

(i) $\zeta_a'|_{\alpha=0}$ denotes damping ratio of the additional system for $\alpha = 0$ with nominal ductility coefficient μ_a. $\zeta_a'|_{\alpha=0}$ can be derived as follows, and the corresponding calculation diagram has been depicted in Fig. B1.

$$E_{Da}|_{\alpha=0} = 4u_{b,\max}^* K_b^*(u_{\max} - u_{b,\max}^*) \tag{94}$$

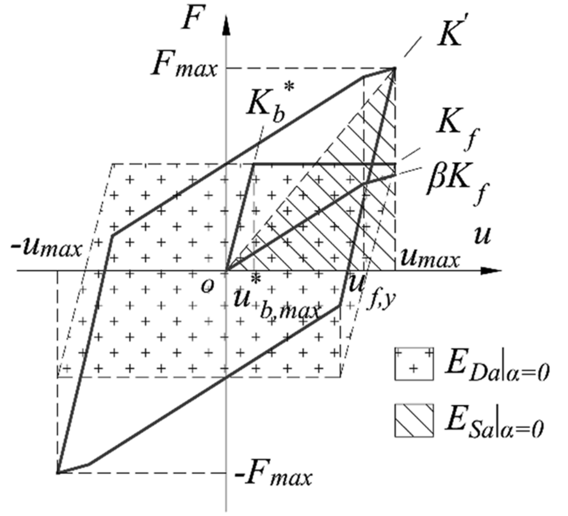

Fig. B1. Calculation diagram for $\zeta_a'|_{\alpha=0}$.

$$E_{Sa}|_{\alpha=0} = \frac{1}{2}u_{f,\max}[u^*_{b,max}K_b^* + u_{fy}K_f + (u_{\max} - u_{fy})\beta K_f] \tag{95}$$

where $E_{Da}|_{\alpha=0}$ denotes the energy dissipated by the additional system for $\alpha = 0$ in one cycle of the reciprocating movement, whereas $E_{Sa}|_{\alpha=0}$ denotes the maximum strain energy of the inelastic analytical model for $\alpha = 0$. For $u_{a,\max} = u_{f,\max}$, $\zeta_a'|_{\alpha=0}$ can be expressed as

$$\zeta_a'|_{\alpha=0} = \frac{E_{Da}|_{\alpha=0}}{4\pi E_{Sa}|_{\alpha=0}} = \frac{2p(\mu_a - 1)}{\pi\mu_a[p + \eta + \beta(\mu_a - \eta)]} \tag{96}$$

$$\eta = u_{fy}/u^*_{b,\max}. \tag{97}$$

(ii) $\zeta_f'|_{\alpha=0}$ denotes damping ratio of the inelastic primary structure for $\alpha = 0$ with maximum ductility coefficient μ_f. An expression for $\zeta_f'|_{\alpha=0}$ can be derived as follows, and the corresponding calculation diagram is depicted in Fig. B2.

$$\begin{aligned} E_{Df}|_{\alpha=0} &= 4\{[K_f u_{fy} + \beta K_f(u_{\max} - u_{fy})]u_{\max} - K_f u_{fy}^2 - \beta K_f(u_{\max} - u_{fy})^2 - 2u_{fy}\beta K_f(u_{\max} - u_{fy})\} \\ &= 4K_f(1 - \beta)u_{fy}(u_{\max} - u_{fy}) \end{aligned} \tag{98}$$

$$E_{Sf}|_{\alpha=0} = E_{Sa}|_{\alpha=0} = \frac{1}{2}u_{\max}[K_b^* u^*_{b,max} + \beta K_f(u_{\max} - u_{fy}) + K_a' u_{\max}] \tag{99}$$

$$\zeta_f'|_{\alpha=0} = \frac{E_{Df}|_{\alpha=0}}{4\pi E_{Sf}|_{\alpha=0}} = \frac{2\eta\rho(1 - \beta)(\mu_f - 1)}{\pi\mu_f[p + \eta + \beta\eta(\mu_f - 1)]} \tag{100}$$

where $E_{Df}|_{\alpha=0}$ denotes the energy dissipated by the inelastic primary structure for $\alpha = 0$ in one cycle of the reciprocating movement while $E_{Sf}|_{\alpha=0}$ denotes maximum strain energy of the inelastic analytical model.

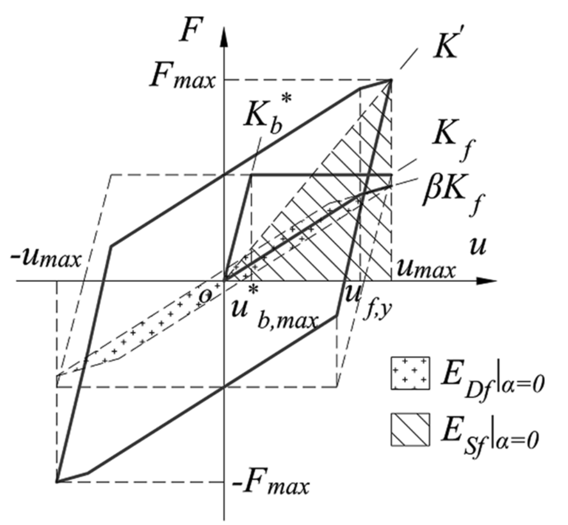

Fig. B2. Calculation diagram for $\zeta_f'\big|_{\alpha=0}$.

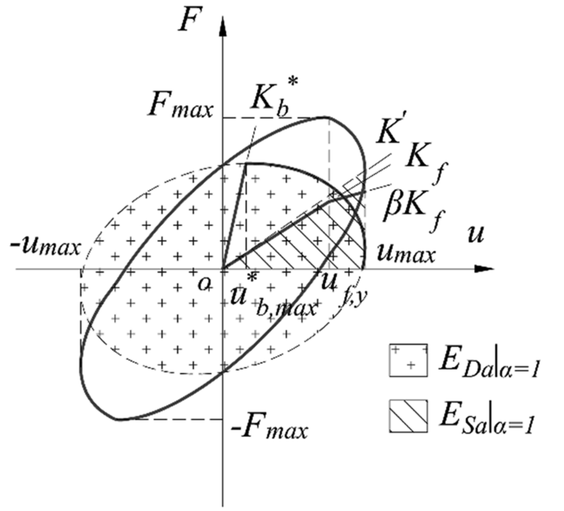

Fig. B3. Calculation diagram for $\zeta_a'|_{\alpha=1}$.

2. For $\alpha = 1$, the equivalent damping ratio $\zeta_{eq}'|_{\alpha=1}$ of the inelastic analytical model can be expressed as

$$\zeta_{eq}'\Big|_{\alpha=1} = \zeta_0 + \zeta_a'\Big|_{\alpha=1} + \zeta_f'\Big|_{\alpha=1} \tag{101}$$

(i) $\zeta_a'|_{\alpha=1}$ denotes damping ratio of the additional system for $\alpha = 1$ with the maximum nominal ductility coefficient μ_a. $\zeta_f'|_{\alpha=1}$ can be derived as follows, and the corresponding calculation diagram is depicted in Fig. B3.

$$E_{Da}|_{\alpha=1} = \pi K_b^* u_{b,\max}^* u_{\max} = \pi\sqrt{\frac{m^2}{m^2+1}} K_b^* u_{b,\max}^* u_{\max} \tag{102}$$

$$\begin{aligned} E_{Sa}|_{\alpha=1} &= \tfrac{1}{2}u_{\max}\left[K_a u_{\max} + K_f u_{fy} + \beta K_f(u_{\max} - u_{fy})\right] \\ &= \tfrac{1}{2}u_{\max}\left[K_b^* \tfrac{1}{1+m^2}u_{\max} + K_f u_{fy} + \beta K_f(u_{\max} - u_{fy})\right] \end{aligned} \tag{103}$$

where $E_{Df}|_{\alpha=1}$ denotes the energy dissipated by the additional system for $\alpha = 1$ in one cycle of reciprocating movement, whereas $E_{Sa}|_{\alpha=1}$ denotes maximum strain energy of the inelastic analytical model for $\alpha = 1$. For $u_{a,\max} = u_{f,\max}$, $\zeta_a'|_{\alpha=1}$ can be expressed as

$$\zeta_a'|_{\alpha=1} = \frac{E_{Da}|_{\alpha=1}}{4\pi E_{Sa}|_{\alpha=1}} = \frac{pm\sqrt{1+m^2}}{2\eta\{[p+\beta(1+m^2)]\mu_f + (1-\beta)(1+m^2)\}}. \tag{104}$$

(ii) $\zeta_f'|_{\alpha=1}$ denotes damping ratio of the inelastic primary structure for $\alpha = 1$ with maximum ductility coefficient μ_f. An expression for $\zeta_f'|_{\alpha=1}$ can be derived as follows with the corresponding calculation diagram being depicted in Fig. B4.

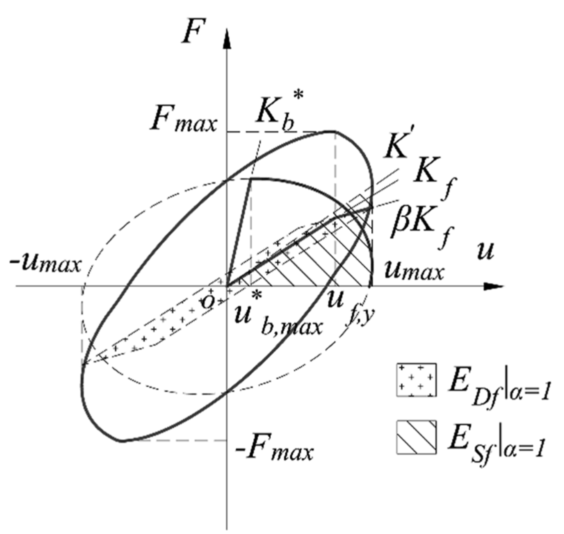

Fig. B4. Calculation diagram for $\zeta_f'\Big|_{\alpha=1}$.

$$E_{Df}|_{\alpha=1} = 4\{[K_f u_{fy} + \beta K_f(u_{\max} - u_{fy})]u_{\max} - K_f u_{fy}^2 - \beta K_f(u_{\max} - u_{fy})^2 - 2u_{fy}\beta K_f(u_{\max} - u_{fy})\}$$
$$= 4K_f(1-\beta)u_{fy}(u_{\max} - u_{fy}) \tag{105}$$

$$E_{Sf}|_{\alpha=1} = E_{Sa}|_{\alpha=1} = \frac{1}{2}u_{f,\max}\left[K_b^*\frac{1}{1+m^2}u_{a,\max} + K_f u_{fy} + \beta K_f(u_{f,\max} - u_{fy})\right] \tag{106}$$

$$\zeta_f'|_{\alpha=1} = \frac{E_{Df}|_{\alpha=1}}{4\pi E_{Sf}|_{\alpha=1}} = \frac{2\rho(1-\beta)(1+m^2)(\mu_f-1)}{\pi\mu_f\{[p+\beta(1+m^2)]\mu_f + (1-\beta)(1+m^2)\}} = \frac{2\rho(1-\beta)(1+m^2)(\mu_f-1)}{\pi\mu_f(z\mu_f+w)} \tag{107}$$

References

[1] Symans MD, Charney FA, Whittaker AS, Constantinou MC, Kircher CA, Johnson MW, et al. Energy dissipation systems for seismic applications: Current practice and recent developments. J Struct Eng 2008;134(1):3–21. https://doi.org/10.1061/(ASCE)0733-9445(2008) 134:1(3).

[2] Manual JSSI. Design and construction manual for passively contolled buildings. Tokyo (Japan): Japan Society of Seismic Isolation; 2007. [in Japanese].

[3] Pan C, Zhang RF. Design of structure with inerter system based on stochastic response mitigation ratio. Struct Control Health Monit 2018;25:e2169. https://doi.org/10.1002/stc.2169.

[4] Pan C, Zhang RF, Luo H, Li C, Shen H. Demand-based optimal design of oscillator with parallel-layout viscous inerter damper. Struct Control Health Monit 2018;25:e2051. https://doi.org/10.1002/stc.2051.

[5] Zhang RF, Zhao Z, Dai KS. Seismic response mitigation of a wind turbine tower using a tuned parallel inerter mass system. Eng Struct 2019;180:29–39. https://doi.org/10.1016/j.engstruct.2018.11.020.

[6] Uriz P, Whittaker AS. Retrofit of pre-northridge steel moment-resisting frames using fluid viscous dampers. Struct Design Tall Build 2001;10(5):371–90. https://doi.org/10.1002/tal.199.

[7] Mcnamara RJ, Taylor DP. Fluid viscous dampers for high-rise buildings. Struct Design Tall Spec Build 2010;12(2):145–54. https://doi.org/10.1002/tal.218.

[8] Wang SS, Lai JW, Schoettler MJ, Mahin SA. Seismic retrofit of a high-rise steel moment resisting frame using fluid viscous dampers. Proc ATC and SEI conference on improving the seismic performance of existing buildings and other structures. 2015.

[9] Huang HC. Efficiency of the motion amplification device with viscous dampers and its application in high-rise buildings. Earthq Eng Eng Vib 2009;8(4):521–36.

[10] Bougteb Y, Ray T. Choice between series and parallel connections of hysteretic system and viscous damper for seismic protection of structures. Earthq Eng Struct Dyn 2018;47(1):237–44. https://doi.org/10.1002/eqe.2938.

[11] Del Gobbo GM, Williams MS, Blakeborough A. Comparing fluid viscous damper placement methods considering total-building seismic performance. Earthq Eng Struct Dyn 2018;47(14):2864–86. https://doi.org/10.1002/eqe.3117.

[12] Pollini N, Lavan O, Amir O. Optimization-based minimum-cost seismic retrofitting of hysteretic frames with nonlinear fluid viscous dampers. Earthq Eng Struct Dyn 2018;47(15):2985–3005. https://doi.org/10.1002/eqe.3118.

[13] Tabar AM. Linearization of seismic response of structures equipped with nonlinear viscous dampers using perturbation technique. Eng Struct 2019;184:459–68. https://doi.org/10.1016/j.engstruct.2019.01.112.

[14] Reinhorn AM, Li C, Constantinou MC. Experimental and analytical investigation of seismic retrofit of structures with supplemental damping, part 1 fluid viscous damping devices Technical Report NCEER-92-0001 ISSN 1088–3800 National Center For Earthquake Engineering Research; 1995.

[15] Constantinou MC, Symans MD. Experimental and analytical investigation of seismic response of structures with supplemental fluid viscous dampers Technical Report NCEER-92-0032 National Center For Earthquake Engineering Research; 1992

[16] Lee D, Taylor DP. Viscous damper development and future trends. Struct Design Tall Build 2001;10(5):311–20. https://doi.org/10.1002/tal.188.

[17] Weng DG, Zhang C, Lu XL, Zeng S, Zhang SM. A simplified design procedure for seismic retrofit of earthquake-damaged RC frames with viscous dampers. Struct Eng Mech 2012;44(5):611–31.

[18] Sadek F, Mohraz B, Riley MA. Linear procedures for structures with velocity-dependent dampers. J Struct Eng 2000;126(8):887–95. https://doi.org/10.1061/(ASCE)0733-9445(2000)126:8(887).

[19] Palermo M, Muscio S, Silvestri S, Landi L, Trombetti T. On the dimensioning of viscous dampers for the mitigation of the earthquake-induced effects in moment-resisting frame structures. B Earthq Eng 2013;11(6):2429–46. https://doi.org/10.1007/s10518-013-9474-z.

[20] Silvestri S, Gasparini G, Trombetti T. A five-step procedure for the dimensioning of viscous dampers to be inserted in building structures. J Earthq Eng 2010;14(3):417–47. https://doi.org/10.1080/13632460903093891.

[21] Silvestri S, Palermo M, Trombetti T. A direct procedure for the seismic design of frame structures with added viscous dampers. Int J Saf Security Eng 2017;7(4):498–509. https://doi.org/10.2495/SAFE-V7-N4-498-509.

[22] Dall'Asta A, Scozzese F, Ragni L, Tubaldi E. Effect of the damper property variability on the seismic reliability of linear systems equipped with viscous dampers. B Earthq Eng 2017;15:5025–53. https://doi.org/10.1007/s10518-017-0169-8.

[23] Pekcan G, Mander JB, Chen SS. Fundamental considerations for the design of non-linear viscous dampers. Earthq Eng Struct Dyn 1999;28(11):1405–25. https://doi.org/10.1002/(SICI)1096-9845(199911)28:11<1405::AID-EQE875>3.0.CO;2-A.

[24] Kim J, Choi H, Min KW. Performance-based design of added viscous dampers using capacity spectrum method. J Earthq Eng 2003;7(1):1–24. https://doi.org/10.1080/13632460309350439.

[25] Lin YY, Tsai MH, Hwang JS, Chang KC. Direct displacement-based design for building with passive energy dissipation systems. Eng Struct 2003;25(1):25–37. https://doi.org/10.1016/S0141-0296(02)00099-8.

[26] Chang KC, Lin YY, Chen CY. Shaking table study on displacement-based design for seismic retrofit of existing buildings using nonlinear viscous dampers. J Struct Eng 2008;134(4):671–81. https://doi.org/10.1061/(ASCE)0733-9445(2008) 134:4(671).

[27] Kim J, Choi H. Displacement-based design of supplemental dampers for seismic retrofit of a framed structure. J Struct Eng 2006;132(6):873–83. https://doi.org/10.1061/(ASCE)0733-9445(2006)132:6(873).

[28] Hejazi F, Shoaei MD, Jaafar MS, Rashid RSBM. Effect of viscous dampers on yielding mechanisms of RC structures during earthquake. Earthq Struct 2015;8(6):1499–528. https://doi.org/10.12989/eas.2015.8.6.1499.

[29] Jack WWG, Christopoulos C. Performance spectra based method for the seismic design of structures equipped with passive supplemental damping systems. Earthq Eng Struct Dyn 2013;42(6):935–52. https://doi.org/10.1002/eqe.2261.

[30] Takewaki I, Yoshitomi S, Uetani K, Tsuji M. Non-monotonic optimal damper placement via steepest direction search. Earthq Eng Struct Dyn 1999;28(6):655–70. https://doi.org/10.1002/(SICI)1096-9845(199906)28:6<655::AID-EQE833>3.0.CO;2-T.

[31] Garcia DL. A simple method for the design of optimal damper configurations in MDOF structures. Earthq Spectra 2001;17(3):387–98. https://doi.org/10.1193/1.1586180.

[32] Aguirre JJ, Almazán JL, Paul CJ. Optimal control of linear and nonlinear asymmetric structures by means of passive energy dampers. Earthq Eng Struct Dyn 2013;42(3):377–95. https://doi.org/10.1002/eqe.2211.

[33] Singh MP, Verma NP, Moreschi LM. Seismic analysis and design with maxwell dampers. J Eng Mech 2003;129(3):273–82. https://doi.org/10.1061/(ASCE)0733-9399(2003) 129:3(273).

[34] Singh MP, Moreschi LM. Optimal seismic response control with dampers. Earthq Eng Struct Dyn 2001;30(4):553–72. https://doi.org/10.1002/eqe.23.

[35] Fujita K, Yamamoto K, Takewaki I. An evolutionary algorithm for optimal damper placement to minimize interstorey-drift transfer function in shear building. Earthq Struct 2010;1(3):289–306. https://doi.org/10.12989/eas.2010.1.3.289.

[36] Lavan O, Levy R. Optimal design of supplemental viscous dampers for linear framed structures. Earthq Eng Struct Dyn 2006;35(3):337–56. https://doi.org/10.1002/eqe.524.

[37] Lavan O. Optimal design of viscous dampers and their supporting members for the seismic retrofitting of 3D irregular frame structures. J Struct Eng 2015;141(11):04015026. https://doi.org/10.1061/(ASCE)ST.1943-541X.0001261.

[38] Lavan O, Dargush GF. Multi-objective evolutionary seismic design with passive energy dissipation systems. J Earthq Eng 2009;13(6):758–90. https://doi.org/10.1080/13632460802598545.

[39] Singh MP, Moreschi LM. Optimal placement of dampers for passive response control. Earthq Eng Struct Dyn 2002;31(4):955–76. https://doi.org/10.1002/eqe.132.

[40] Wongprasert N, Symans MD. Application of a genetic algorithm for optimal damper distribution within the nonlinear seismic benchmark building. J Eng Mech 2004;130(4):401–6. https://doi.org/10.1061/(ASCE)0733-9399(2004) 130:4(401).

[41] Lin TK, Hwang JS, Chen KH. Optimal distribution of damping coefficients for viscous dampers in buildings. Int J Struct Stab Dyn 2017;17(4):1–18. https://doi.org/10.1142/S0219455417500547.

[42] Halperin I, Agranovich G, Ribakov Y. Efficient newton method for optimal viscous dampers design. Proc IEEE 28th convention of electrical and electronics engineers in Israel. 2014.

[43] Halperin I, Ribakov Y, Agranovich G. Optimal viscous dampers gains for structures subjected to earthquakes. Struct Control Health Monit 2016;23(3):458–69. https://doi.org/10.1002/stc.1779.

[44] Milman MH, Chu CC. Optimization methods for passive damper placement and tuning. J Guid Control Dyn 2007;17(4):848–56.

[45] Su C, Li B, Chen T, Dai X. Stochastic optimal design of nonlinear viscous dampers for large-scale structures subjected to non-stationary seismic excitations based on dimension-reduced explicit method. Eng Struct 2018;175:217–30. https://doi.org/10.1016/j.engstruct.2018.08.028.

[46] Xie Y, Zhang J, Xi W. Effectiveness evaluation and optimal design of nonlinear

viscous dampers for inelastic structures under pulse-type ground motions. Earthq Eng Struct Dyn 2018;47(14):2802–20. https://doi.org/10.1002/eqe.3109.
[47] Huang X. Evaluation of genetic algorithms for the optimum distribution of viscous dampers in steel frames under strong earthquakes. Earthq Struct 2018;14(3):215–27. https://doi.org/10.12989/eas.2018.14.3.215.
[48] Altieri D, Tubaldi E, Angelis MD, Patelli E, Dall'Asta A. Reliability-based optimal design of nonlinear viscous dampers for the seismic protection of structural systems. B Earthq Eng 2018;16(2):963–82. https://doi.org/10.1007/s10518-017-0233-4.
[49] Miyamoto HK, Gilani ASJ, Wada A, Ariyaratana C. Limit states and failure mechanism of viscous dampers and implications for large earthquakes. Earthq Eng Struct Dyn 2010;39(11):1279–97. https://doi.org/10.1002/eqe.993.
[50] Zhang L, Su MZ, Zhang C, Shen H, Islam MM, Zhang RF. A design method of viscoelastic damper parameters based on the elastic-plastic response reduction curve. Soil Dyn Earthq Eng 2019;117:149–63. https://doi.org/10.1016/j.soildyn.2018.09.050.
[51] Shen H, Zhang RF, Weng DG, Gao C, Luo H, Pan C. Simple design method of structure with metallic yielding dampers based on elastic–plastic response reduction curve. Eng Struct 2017;150:98–114. https://doi.org/10.1016/j.engstruct.2017.07.047.
[52] Chopra AK. Dynamics of structures theory and applications to earthquake engineer. 4th ed. Boston: Prentice Hall; 2012.
[53] ATC-40. Seismic evaluation and retrofit of concrete building. Redwood City (CA): Applied Technology Council; 1996.
[54] Kasai K, Okuma K. Evaluation rule and its accuracy for equivalent period and damping of frequency-dependent and passive control system. J Struct Constr Eng, AIJ 2004;580:51–9. [in Japanese].
[55] GB 50011-2010. Code for seismic design of building. Beijing: The Ministry of Housing and Urban-Rural Construction of the People's Republic of China; 2010.
[56] Adachi F, Fujita K, Tsuji M, Takewaki I. Importance of interstory velocity on optimal along-height allocation of viscous oil dampers in super high-rise buildings. Eng Struct 2013;56:489–500. https://doi.org/10.1016/j.engstruct.2013.05.036.
[57] Hao LF, Zhang RF, Jin K. Direct design method based on seismic capacity redundancy for structures with metal yielding dampers. Earthq Eng Struct Dyn 2018;47(2):515–34. https://doi.org/10.1002/eqe.2977.
[58] Zhang RF, Wang C, Pan C, Shen H, Ge QZ, Zhang LQ. Simplified design of elastoplastic structures with metallic yielding dampers based on the concept of uniform damping ratio. Eng Struct 2018;176:734–45. https://doi.org/10.1016/j.engstruct.2018.09.009.
[59] User guide of nolinear analysis and performance assessment for 3D structures. Computers and Structures Inc; 2018.
[60] GB 50017-2017. Code for design of steel structures. Beijing: The Ministry of Housing and Urban-Rural Construction of the People's Republic of China; 2017.
[61] PEER. Peer ground motion database. Pacific Earthquake Engineering Research Center; 2018.
[62] Pan C, Zhang RF, Luo H, Shen H. Target-based algorithm for baseline correction of inconsistent vibration signals. J Vib Control 2018;24(12):2562–75. https://doi.org/10.1177/1077546316689014.
[63] Freddi F, Tubaldi E, Ragni L, Dall'Asta A. Probabilistic performance assessment of low-ductility reinforced concrete frames retrofitted with dissipative braces. Earthq Eng Struct Dyn 2012;42(7):993–1011. https://doi.org/10.1002/eqe.2255.